

# First Year Report

07 September 2009

**Valeriu Predoi**

Department of Physics and Astronomy  
Cardiff University  
The Parade  
CF24 1AA Cardiff  
United Kingdom

**Supervisor:** Dr. Stephen Fairhurst

# Contents

<b>1</b>	<b>Introduction</b>	<b>3</b>
<b>2</b>	<b>Gravitational Waves Theory</b>	<b>3</b>
2.1	Introducing Gravitational Waves . . . . .	3
2.2	Linearized theory of Gravitational Waves produced by a binary system of coalescing compact stars . . . . .	5
<b>3</b>	<b>Detectors of Gravitational Waves</b>	<b>10</b>
<b>4</b>	<b>Data Analysis Procedures</b>	<b>12</b>
4.1	Matched Filtering . . . . .	12
4.2	$\chi^2$ test . . . . .	14
<b>5</b>	<b>Short Hard Gamma Ray Burst GRB070429B analyzed by the inspiral pipeline</b>	<b>15</b>
5.1	Introducing GRB070429B . . . . .	15
5.2	The Data Analysis from GRB070429B . . . . .	16
5.3	Future work . . . . .	20
<b>6</b>	<b>Perspectives on joint detection of GW and radio transients</b>	<b>21</b>
6.1	Introduction . . . . .	21
6.2	Theoretical Models for radio emission before merger . . . . .	22
6.3	Gamma ray burst afterglows . . . . .	26
6.4	Unidentified radio transients . . . . .	26
6.5	Transients follow-up and the LOFAR telescope . . . . .	26
6.6	Future work . . . . .	27
<b>7</b>	<b>Nested Sampling - A New Coherent Approach</b>	<b>27</b>
7.1	Introducing the Nested Sampling data analysis algorithm . . . . .	27
7.2	<i>LALAPPS_INSPNEST</i> on data from GRB070429B - preliminaries . . . . .	28
7.3	Future work . . . . .	31

## Abstract

blah...



# 1 Introduction

The elusive nature of gravitational waves (GW), first predicted by Albert Einstein almost a century ago, is, nowadays, closer than ever to be unveiled - science has never been this ready for a gravitational waves detection and hopes are very high for the occurrence such an event in the next few years. I joined the gravitational waves Cardiff search group last September, embarking on my first year of PhD, under the supervision of Dr. Stephen Fairhurst. Initially, my attention was focused on actually understanding the theory behind gravitational waves, as it is laid down as part of General Relativity. I have come to grips with the most basic derivations and gradually tried to understand the linearized theory of GW, in the same time starting to read about data analysis techniques and the involved detectors. All my knowledge on this side is presented in the second, third and fourth chapters of this report, following the Introduction.

From the very beginning of my PhD, the focus has been geared towards an effort of understanding gravitational waves and electromagnetic phenomenae produced by binary inspiralling compact objects. Coincident detection of these two apparently independent physical manifestations of the inspiralling process, if materialized, will improve both the detection sensitivity itself and the parameter estimation. The first step I took to actually work on real GW data was by analyzing the short hard GRB070429B. Short GRBs are extragalactic strong flashes of  $\gamma$  radiation easily detectable on Earth having progenitors believed to be mergers of two inspiralling compact objects (either two neutron stars or a neutron star and a black hole). The analysis started in October 2008 and continued until March 2009 due to constant upgrades of the code used for the analysis. The analysis results are presented in detail in Section Five.

Understanding gravitational waves means firstly understanding the sources and a greater diversity of putative sources translates into greater chances of a GW detection. Following my supervisors suggestion, I started researching the possibility of having coincident GW-radio transients searches. The primary motivation was that transient radio skies are poorly explored and there is an abundance of theoretical literature predicting radio signals emitted before or after the merger of two compact objects in the form of transients, detectable on Earth with the new generation of radio arrays. The secondary reason for me to start such a project was that it simply sounded very exciting! The first step I took was to search and find as many scientific articles as possible predicting a prompt radio emission as a consequence of a binary merger. The selected reading is presented in Section Six.

Apart from starting to look at a new class of sources, the last two months worth of effort has been put towards testing a new coherent analysis pipeline - the nested sampling algorithm. Testing it means analyzing parts of real GW data collected from the GRB070429B and comparing the results with the inspiral pipeline output. A coherent analysis has the advantage of simultaneously using data from as many GW detectors as one has available and is also a very powerful parameter estimator. The test run results I have collected up to now are presented in Section Seven.

## 2 Gravitational Waves Theory

### 2.1 Introducing Gravitational Waves

Gravitational waves are waves in the space-time fabric and are a direct consequence of Albert Einsteins General Theory of Relativity. First introduced in 1916, gravitational waves had to wait for about six decades to have their physical existence confirmed in an indirect way (see the famous binary pulsar PSR1913+16, described below) and are still awaiting a direct detection.

Gravitational waves resemble electromagnetic waves in several aspects. They propagate at the light speed  $c$ , have two independent transverse polarisation states (the  $+$  and  $\times$  polarizations, see Linearized Theory section) and their action on masses is similar to electromagnetic waves action on charges. Gravitational waves carry away energy, angular momentum and linear momentum from the radiating source.

Like electromagnetic waves, which are mainly dipolar radiation, gravitational waves are mainly quadrupolar radiation, the leading term in generation being a time-varying mass quadrupole. There are no mass monopoles or dipoles involved in the radiation process and the contribution of octupoles and higher order terms will be neglected in the calculations that follow.

The gravitational wave field is dimensionless, and its strength is qualitatively characterized by a single quantity called the gravitational wave amplitude or strain  $h$ . The amplitude falls off during propagation from a localized source, in proportion to the inverse power of the traveled distance  $D$

according to  $h \sim 1/D$ . The difficulty of direct detection of gravitational waves can be seen from the fact that the expected amplitude (or strain in a GW detector)  $h$  on Earth from close-by astronomical sources is exceedingly small, of the order of or smaller than  $10^{-21}$ . Hence, the only way to prove the existence of gravitational waves is to measure this amplitude  $h$  in the form of a strain applied by the wave on a series of test masses (see the *Detectors* section below).

According to different gravitational wave progenitors and different observational and analysis techniques, there are several types of GW sources. Here is a brief list of sources:

- **Coalescing binaries of compact stars - the Chirp Signals** The chirp signal will be produced by two compact objects orbiting each other around the common center of mass (two neutron stars, two black holes or a black hole and a neutron star). The binary system will lose energy and angular momentum due to emission of gravitational waves, gradually decreasing the separation between the components and increasing the orbital frequency. This process is very lengthy (order of  $\sim \text{Gyr}$ , [REF]) but the very last orbits before merger can be completed in very short times (fractions of seconds) and it is then when the bulk of gravitational waves energy is released. The signal detectable on Earth will be a *chirp wave*. It will resemble a chirp in that the frequency and amplitude will increase as the two objects coalesce. This signal will be characterized by the masses radial separation and eccentricity of the two orbiting bodies. The search for gravitational waves from such objects is performed in a *modelled* way by analytically or numerically constructing the inspiral waveforms and matching the observational data with them.
- **Burst Signals** Burst (or transient) events are responsible for the release of a great amount of gravitational energy over a short period of time. It is believed that this type of signal will result from a short hard gamma ray burst, the non-axial collapse of a super nova or even from a star crossing the event horizon of a black hole. These types of sources are treated as *unmodelled* in the burst search and the search is performed over any highly energetic gravitational wave event no matter its specific progenitor, thus having the opportunity of discovering new burst sources.
- **Stochastic Background Radiation** Similar to the cosmic microwave background and the unprobed cosmic neutrino background there exists a cosmic gravitational wave background. As an echo of the Big Bang itself and a superposition of the radiation from all the cosmic past and present sources, it goes all the way back to the end of Planck time and therefore may be one of the best indicators of the early universe. Unfortunately, the wave amplitudes are still ambiguous and a detection is still hindered by theoretical confusion.
- **Periodic Signals** Periodic gravitational wave sources emit continuous, almost monochromatic waves, for very long intervals of time. Nonasymmetric motion of neutron stars (e.g. a spherical neutron star with a large mountain) can be tracked over many cycles to produce a periodic signal of such gravitational waves. Through these observations, the gradual slowing of a pulsar (neutron star having a strong magnetic field) spin can be monitored. The waves can be used to monitor existing pulsars and do search of the sky to find unknown pulsars. The continuous wave sensitivity search is improved as the time of observation increases.

As stated above, there is no direct observation of gravitational waves as of yet, but there is a series of indirect proofs of their existence. The most solid experimental argument was brought by the discovery of the pulsar PSR1913+16, observed by Russell Hulse and Joseph Taylor of Princeton University in 1974. Both physicists have been awarded the Nobel Prize for Physics in 1993 for this discovery. PSR1913+16 is a binary pulsar (with relatively low eccentricity) and the separation between components has decreased over a span of 36 years in exact accordance with Einstein's relativity theory. According to this, the binary components lose energy and angular momentum due to emitting gravitational waves. Figure 1 is a diagram showing how exact is the relativistically predicted decrease (continuous line) compared to the actual data points.

For the rest of this report, I will concentrate on the first type of source, the coalescing compact binaries, due to the fact that all my work and analysis has been done and will pursue as part of the Compact Binaries Collaboration (CBC), that aims at detecting gravitational waves from this very type of source.

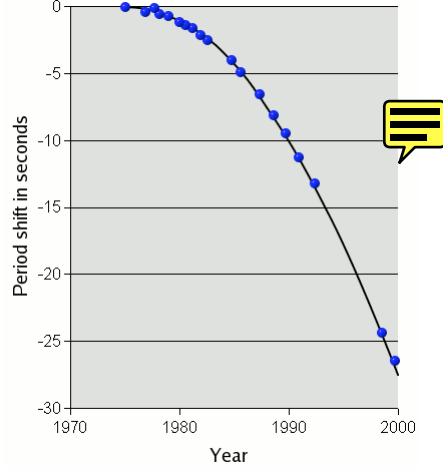


Figure 1: The periastron period shift plotted against time, for the Hulse-Taylor PSR1913+16 binary pulsar. The companion arrives earlier at the periastron due to the decrease in separation, hence showing a decrease of the orbital period.

## 2.2 Linearized theory of Gravitational Waves produced by a binary system of coalescing compact stars

Gravitational waves can be naively seen as *ripples* in the space-time fabric created by a strong gravitational field source. As the first assumptions we consider placing the observer far away from that putative source and considering that the gravitational field at the observer is weak but not static, and that there are no restrictions on the motion of particles in the vicinity of the observer. In the absence of gravitational interaction, space-time is flat and is characterised by the Minkowski flat metric,  $\eta_{\mu\nu} = \text{diag}(-1, 1, 1, 1)$ . A weak gravitational field can be considered as a small 'perturbation' on the flat Minkowski metric [REF],

$$g_{\mu\nu} = \eta_{\mu\nu} + h_{\mu\nu}, \quad |h_{\mu\nu}| \ll 1 \quad (1)$$

The condition  $||h_{\mu\nu}|| \ll 1$  shows that the analysis is done in a weak gravitational field. Here  $||h_{\mu\nu}||$  is defined as the magnitude of a typical non-zero component of  $h_{\mu\nu}$ . In linearized gravity, the smallness of the perturbation means that we only keep terms which are linear in  $h_{\mu\nu}$ , higher order terms are discarded. As a consequence, indices are raised and lowered using the flat metric  $\eta_{\mu\nu}$ . The metric perturbation  $h_{\mu\nu}$  transforms as a tensor under Lorentz transformations. We can therefore write,

$$g^{\mu\nu} = \eta^{\mu\nu} - h^{\mu\nu} \quad (2)$$

Under a background Lorentz transformation [REF], the perturbation transforms as a second-rank tensor:

$$h_{\alpha\beta} = \Lambda_{\alpha}^{\mu} \Lambda_{\beta}^{\nu} h_{\mu\nu} \quad (3)$$

The equations obeyed by the perturbation,  $h_{\mu\nu}$ , are obtained by writing the Einstein's equations to first order. To the first order, the Christoffel symbol is,

$$\Gamma^{\lambda}_{\mu\nu} = \frac{1}{2} \eta^{\lambda\rho} [\partial_{\mu} h_{\rho\nu} + \partial_{\nu} h_{\mu\rho} - \partial_{\rho} h_{\mu\nu}] + \mathcal{O}(h^2) \quad (4)$$

Therefore, the Riemann curvature tensor will reduce to

$$R_{\mu\nu\rho\sigma} = \eta_{\mu\lambda} \partial_{\rho} \Gamma^{\lambda}_{\nu\sigma} - \eta_{\mu\lambda} \partial_{\sigma} \Gamma^{\lambda}_{\nu\rho} \quad (5)$$

The Ricci tensor is obtained to the first order as follows:

$$R_{\mu\nu} \approx R_{\mu\nu}^{(1)} = \frac{1}{2} [\partial_{\lambda} \partial_{\nu} h^{\lambda}_{\mu} + \partial_{\lambda} \partial_{\mu} h^{\lambda}_{\nu} - \partial_{\mu} \partial_{\nu} h - \square h_{\mu\nu}] \quad (6)$$

where,  $\square = \eta^{\lambda\rho}\partial_\lambda\partial_\rho$  is the D'Alembertian in flat space-time. Contracting with  $\eta^{\mu\nu}$ , the Ricci scalar is obtained as follows:

$$R = \partial_\lambda\partial_\mu h^{\lambda\mu} - \square h \quad (7)$$

The Einstein tensor,  $G_{\mu\nu}$ , in the limit of weak gravitaty is

$$G_{\mu\nu} = R_{\mu\nu} - \frac{1}{2}\eta_{\mu\nu}R = \frac{1}{2}[\partial_\lambda\partial_\nu h^\lambda_\mu + \partial_\lambda\partial_\mu h^\lambda_\nu - \eta_{\mu\nu}\partial_\mu\partial_\nu h^{\mu\nu} + \eta_{\mu\nu}\square h - \square h_{\mu\nu}] \quad (8)$$

The Einstein equations read:

$$G_{\mu\nu} = R_{\mu\nu} - \frac{1}{2}\eta_{\mu\nu}R = \frac{8\pi G}{c^4}T_{\mu\nu} \quad (9)$$

For simplicity one can choose  $c = 1$ . The decomposition (1) of  $g_{\mu\nu}$  in the weak gravitational field approximation allows for a choice of coordinate systems, not specifying the any privileged system. When one has a system that is invariant under a gauge transformation, one can fix the gauge and work in a chosen coordinate system. One such coordinate system is the Lorentz gauge coordinate system [REF]. The gauge condition is called *Lorentz gauge*:

$$g^{\mu\nu}\Gamma^\lambda_{\mu\nu} = 0 \quad (10)$$

In the weak field limit, this condition reduces to

$$\partial_\lambda h^\lambda_\mu = \frac{1}{2}\partial_\mu h \quad (11)$$

In this chosen gauge, the linearized Einstein equations simplify to:

$$\square h_{\mu\nu} - \frac{1}{2}\eta_{\mu\nu}\square h = -16\pi GT_{\mu\nu} \quad (12)$$

The trace-reversed perturbation,  $\bar{h}_{\mu\nu}$ , is defined as follows:

$$\bar{h}_{\mu\nu} = h_{\mu\nu} - \frac{1}{2}\eta_{\mu\nu}h \quad (13)$$

The Lorentz gauge condition further reduces to:

$$\partial_\mu \bar{h}^\mu_\lambda = 0 \quad (14)$$

The Einstein equations are then:

$$\square \bar{h}_{\mu\nu} = -16\pi GT_{\mu\nu} \quad (15)$$

The above equation is written in the presence of matter and energy. If written in vacuum, where the stress-energy tensor will vanish, we obtain the familiar plane waves equation:

$$\square \bar{h}_{\mu\nu} = 0 \quad (16)$$

The vacuum equations for  $\bar{h}_{\mu\nu}$  are similar to the wave equations in electrodynamics or acoustics. These second order partial differential equations will have plane-wave solutions of the type:

$$\bar{h}_{\mu\nu} = B_{\mu\nu}\exp(ik_\alpha x^\alpha) \quad (17)$$

where,  $B_{\mu\nu}$  is a constant, symmetric second rank tensor and  $k_\alpha$  is a constant four-vector known as the *plane wave vector*. The waves are propagating with a group velocity  $c = 1$  and the dispersion relation will be:

$$\omega^2 = |\mathbf{k}|^2 \quad (18)$$

Using the Lorentz gauge condition (14), one obtains as follows:

$$k_\alpha B^{\alpha\beta} = 0 \quad (19)$$

This imposes a restriction on  $B^{\alpha\beta}$  : it is orthogonal (*transverse*) to  $k_\alpha$ . It can be easily proved that any coordinate transformation of the form

$$x^{\alpha'} = x^\alpha + \xi^\alpha(x^\beta) \quad (20)$$

will leave the plane wave equation

$$\square x^\mu = 0 \quad (21)$$

satisfied as long as

$$\square \xi^\alpha = 0 \quad (22)$$

One can therefore choose a solution

$$\xi_\alpha = C_\alpha \exp(ik_\beta x^\beta) \quad (23)$$

to the wave equation for any  $\xi_\alpha$ .  $C_\alpha$  are constant coefficients. If

$$B_\mu^\mu = 0 \quad (\text{traceless}) \quad (24)$$

and

$$B_{\mu\nu} V^\beta = 0 \quad (25)$$

where,  $V^\beta$  is some fixed four-velocity, that is, any constant time dependent unit vector one wishes to choose. The equations

$$\boxed{k_\alpha B^{\alpha\beta} = 0 \quad B_\mu^\mu = 0 \quad B_{\mu\nu} V^\beta = 0} \quad (26)$$

are called the the *transverse traceless* (TT) gauge conditions [REF]. The trace condition  $B_\mu^\mu = 0$  implies that

$$\bar{h}_{\alpha\beta}^{TT} = h_{\alpha\beta}^{TT} \quad (27)$$

Consider now a background Lorentz transformation in which the vector  $V^\alpha$  is the time basis vector  $V^\alpha = \delta_0^\alpha$ . Then the third TT equation implies that  $B_{\mu 0} = 0$  for all  $\mu$ .

Consider now a privileged orientation of the coordinate axes so that the wave is travelling along the  $z$ -direction,  $k^\mu \rightarrow (\omega, 0, 0, \omega)$ . Then with the TT equations it implies that  $B_{\alpha z} = 0$  for all  $\alpha$ . Thus,  $B_{\alpha\beta}^{TT}$  in matrix form is

$$B_{\alpha\beta}^{TT} = \begin{pmatrix} 0 & 0 & 0 & 0 \\ 0 & B_{xx} & B_{xy} & 0 \\ 0 & B_{xy} & -B_{xx} & 0 \\ 0 & 0 & 0 & 0 \end{pmatrix} \quad (28)$$

The  $xx$  and  $xy$  components of the amplitude tensor are also called the polarizations and labelled as  $xx \equiv +$  and  $xy \equiv \times$  as in the following:

$$\boxed{B_{\alpha\beta}^{TT} = \begin{pmatrix} 0 & 0 & 0 & 0 \\ 0 & B_+ & B_\times & 0 \\ 0 & B_\times & -B_+ & 0 \\ 0 & 0 & 0 & 0 \end{pmatrix}} \quad (29)$$

To obtain the solution of the linearised wave equations, the Green's function method will be used. The Green's function,  $G(x^\mu - y^\mu)$ , of the D'Alembertian operator  $\square$ , is the solution of the wave equation in the presence of a delta function source:

$$\square G(r_1 - r_2) = \delta^{(3)}(r_1 - r_2) \quad (30)$$

where  $\delta^{(3)}$  is the three-dimensional Dirac delta function (stepped over time). The general solution to the linearized Einstein's equations can be written using the Green's function as

$$\bar{h}_{\mu\nu}(t, \mathbf{r}_1) = 4G \int d^3\mathbf{r}_2 \frac{1}{|\mathbf{r}_1 - \mathbf{r}_2|} T_{\mu\nu}(t - |\mathbf{r}_1 - \mathbf{r}_2|, \mathbf{r}_2) \quad (31)$$

The quantity



$$t_r = t - |\mathbf{r}_1 - \mathbf{r}_2| \quad (32)$$

is called the *retarded time* with  $\mathbf{D} = \mathbf{r}_1 - \mathbf{r}_2$ . From the expression for  $\bar{h}_{\mu\nu}$ , it is easy to observe that the perturbation in the gravitational field at  $(t, \mathbf{r}_1)$  is a sum of the influences from the energy and momentum sources at the point  $(t_r, \mathbf{r}_2)$ .

One can now consider the gravitational radiation emitted by an isolated far away source consisting of very slowly moving particles (the spatial dimensions of the source are neglected compared to the distance between the source and the observer). The Fourier transform of the perturbation  $\bar{h}_{\mu\nu}$  is

$$\tilde{\bar{h}}_{\mu\nu}(\omega, \mathbf{r}_1) = \frac{1}{\sqrt{2\pi}} \int dt \exp(i\omega t) \bar{h}_{\mu\nu}(t, \mathbf{r}_1) \quad (33)$$

Using the expression for  $\bar{h}_{\mu\nu}(t, \mathbf{r}_1)$ , one obtains

$$\tilde{\bar{h}}_{\mu\nu} = 4G \int d^3\mathbf{r}_2 \exp(i\omega|\mathbf{r}_1 - \mathbf{r}_2|) \frac{\tilde{T}_{\mu\nu}(\omega, \mathbf{r}_2)}{|\mathbf{r}_1 - \mathbf{r}_2|} \quad (34)$$

Under the assumption that the spatial extent of the source is much smaller compared to the distance between the source and the observer, one can replace the term  $\exp(i\omega|\mathbf{r}_1 - \mathbf{r}_2|)/|\mathbf{r}_1 - \mathbf{r}_2|$  in by  $\exp(i\omega D)/D$ . Therefore,

$$\tilde{\bar{h}}_{\mu\nu}(\omega, \mathbf{r}_1) = 4G \frac{\exp(i\omega D)}{D} \int d^3\mathbf{r}_2 \tilde{T}_{\mu\nu}(\omega, \mathbf{r}_2) \quad (35)$$

The Lorentz gauge condition in Fourier space is

$$\partial_\mu \bar{h}^{\mu\nu}(t, \mathbf{r}_1) = \partial_\mu \int d\omega \tilde{\bar{h}}^{\mu\nu} \exp(-i\omega t) = 0 \quad (36)$$

Separating out the space and time components, using Gauss' theorem:

$$\int d^3\mathbf{r}_2 \tilde{T}^{ij}(\omega, \mathbf{r}_2) = - \int d^3\mathbf{r}_2 r_2^i \left( \partial_k \tilde{T}^{kj} \right) \quad (37)$$

and considering the Fourier space version of the conservation of energy equation for  $T^{\mu\nu}$ , that is,  $\partial_\mu T^{\mu\nu}(t, \mathbf{r}_1) = 0$  and finally introducing the *quadrupole moment tensor* of the energy-density of the source as

$$\tilde{Q}_{ij}(\omega) = \int d^3\mathbf{r}_2 r^i r^j \tilde{T}^{00}(\omega, \mathbf{r}_2) \quad (38)$$

With respect of the newly defined quadrupole moment tensor, we have

$$\int d^3\mathbf{r}_2 \tilde{T}^{ij}(\omega, \mathbf{r}_2) = -\frac{\omega^2}{2} \tilde{Q}_{ij}(\omega) \quad (39)$$

Hence, the solution reads

$$\tilde{\bar{h}}_{ij}(\omega, \mathbf{r}_1) = 4G \frac{\exp(i\omega D)}{D} \left( -\frac{\omega^2}{2} \tilde{Q}_{ij}(\omega) \right) \quad (40)$$

and making further simplifications,

$$\tilde{\bar{h}}_{ij}(\omega, \mathbf{r}_1) = -2 \frac{G\omega^2}{D} \exp(i\omega D) \tilde{Q}_{ij}(\omega) \quad (41)$$

The final expression of the metric perturbation is obtained after a last Fourier transform:

$$\bar{h}_{ij}(t, \mathbf{r}_1) = \frac{2G}{D} \frac{d^2}{dt^2} Q_{ij}(t_r) \quad (42)$$

where,  $t_r = t - |\mathbf{r}_1 - \mathbf{r}_2| = t - D$  is the retarded time. To write this expression in SI units:



$$\boxed{\bar{h}_{ij}(t, \mathbf{r}_1) = \frac{2G}{c^4 D} \frac{d^2}{dt^2} Q_{ij}\left(t - \frac{|\mathbf{r}_1 - \mathbf{r}_2|}{c}\right)} \quad (43)$$

To get a more general solution, we need to remove the  $z$  propagation condition. To obtain the new expression for  $\bar{h}_{ij}(t, \mathbf{r}_1)$  we need to apply a rotation  $\mathbf{R} = \mathbf{R}(\theta, \phi)$  matrix with the new quadrupole moment defined as

$$Q_{ij}^r = \mathbf{R}^T(\theta, \phi) Q_{ij} \mathbf{R}(\theta, \phi) \quad (44)$$

While higher order multipole moments of the mass distribution can contribute to the radiation, for most systems the quadrupole will dominate. Further, the mass monopole and dipole moment will not contribute any gravitational waves. Thus, such events as a spherically symmetric gravitational collapse and axially symmetric rotation do not emit any gravitational radiation. On the other hand, a rotating dumbbell is an excellent emitter of gravitational waves, making binary systems potentially amongst the brightest emitters of waves in the Universe.

Two compact stars (binary neutron stars, neutron star-black hole or binary black holes) orbit each other in a close orbit and due to the very strong gravitational field produced by this high-mass system, gravitational waves are emitted. By emitting gravitational waves, the system loses energy and angular momentum hence the separation between the objects lessens with every orbit. The closer the stars get to each other, more orbital energy is converted into gravitational waves, hence, the stronger the gravitational waves are. This system can be easily modelled analytically, in a Newtonian approximation, as described below.

Lets consider such a system of two inspiralling compact objects, orbiting each other around the common center of mass (CM). The components have masses  $m_1$  and  $m_2$ , orbiting with an angular velocity  $\Omega = \Omega(t)$  and the orbit is considered plane circular and obeying the classical keplerian laws for celestial bodies. The system can be considered in quasi-equilibrium at the time  $t$  much smaller than the coalescence time if

$$\frac{d\Omega(t)}{dt} \ll \Omega^2(t) \quad (45)$$

where  $\Omega = \Omega(t)$  is the orbital frequency.

The separation  $r = r(t)$  between the stars will decrease gradually and reach null value at merger. In plane, cartesian coordinates, the system is described by the position coordinates with respect to CM:

$$x_1(t) = r \cos(\Omega t + \phi_0) \quad x_2(t) = r \sin(\Omega t + \phi_0) \quad x_3(t) = 0 \quad (46)$$

In the center of mass of the system the moment of inertia (the second mass moment) is

$$Q^{ij} = \mu x^i(t) x^j(t) \quad (47)$$

where  $\mu = m_1 m_2 / (m_1 + m_2)$  is the reduced mass. Taking the time derivatives and applying equations 29 and 43 we calculate  $h_{ij} = (h_+, h_\times)$  for the system. It is convenient to introduce the *chirp mass* as follows:

$$M_c = \frac{(m_1 m_2)^{3/5}}{(m_1 + m_2)^{1/5}} \quad (48)$$

A solution of equation (43) in a geocentric reference frame would read:

$$h_+(t) = \frac{4}{D} \left( \frac{GM_c}{c^2} \right)^{5/3} \left[ \frac{\pi f_{gw}(t)}{c} \right]^{2/3} \frac{1 + \cos^2 \theta}{2} \cos(2\pi f_{gw} t_{ret} + 2\phi) \quad (49)$$

$$h_\times(t) = \frac{4}{D} \left( \frac{GM_c}{c^2} \right)^{5/3} \left[ \frac{\pi f_{gw}(t)}{c} \right]^{2/3} \cos \theta \sin(2\pi f_{gw} t_{ret} + 2\phi) \quad (50)$$

where  $f_{gw} = \omega_{gw}/2\pi = 2\Omega/2\pi$  is the frequency of the gravitational wave (double the orbital frequency) and  $t_{ret} \equiv t - D/c$  is the retarded time. The waveforms consist of a time-varying amplitude and a time-varying phase for the two polarizations:

$$A_+(t) = \frac{4}{D} \left( \frac{GM_c}{c^2} \right)^{5/3} \left[ \frac{\pi f_{gw}(t)}{c} \right]^{2/3} \frac{1 + \cos^2 \theta}{2} \quad (51)$$

$$\Phi_+(t) = \Phi_\times(t) = 2\pi f_{gw}(t)t_{ret}(t) + 2\phi \quad (52)$$

$$A_\times = \frac{4}{D} \left( \frac{GM_c}{c^2} \right)^{5/3} \left[ \frac{\pi f_{gw}(t)}{c} \right]^{2/3} \cos \theta \quad (53)$$

The gravitational waves emission causes the loss of orbital energy hence the orbits become shorter with time, the orbital frequency increasing. The gravitational wave will chirp reaching its maximum amplitude and frequency at the merger of the two stars. Considering the equilibrium between the loss of orbital energy and the gain in gravitational energy one can write down the energy conservation law [REF]

$$P_{gw} = \frac{dE_{gw}}{dt} = \frac{32}{5} \frac{c^5}{G} \frac{(GM_c \omega_{gw}(t))^{10/3}}{2^{10/3} c^{10}} \quad (54)$$

and

$$P_{orbit} = \frac{dE_{orbit}}{dt} = -\frac{d}{dt} \frac{G^{2/3} M_c^{5/3} \omega_{gw}^{2/3}(t)}{32^{1/3}} \quad (55)$$

Placing  $P_{gw} = P_{orbit}$  we can solve for  $\omega_{gw} = \omega_{gw}(t)$  and obtain, after a series of calculations:

$$\omega_{gw}(\tau) = \frac{1}{4} \left( \frac{\tau}{5} \right)^{-3/8} \left( \frac{GM_c}{c^3} \right)^{-5/8} \quad (56)$$

where  $\tau \equiv t - t_{coal}$  is the time to coalescence. The shape of the wave is pictured in Figure 2 and represents the newtonian approximation in linear orders of  $v/c$  for the inspiral phase, in other words in weak gravity. The chirp increases its amplitude and frequency (the inspiral phase), reaches the peak (the merger phase) and afterwards it damps down very fast (the ringdown phase).

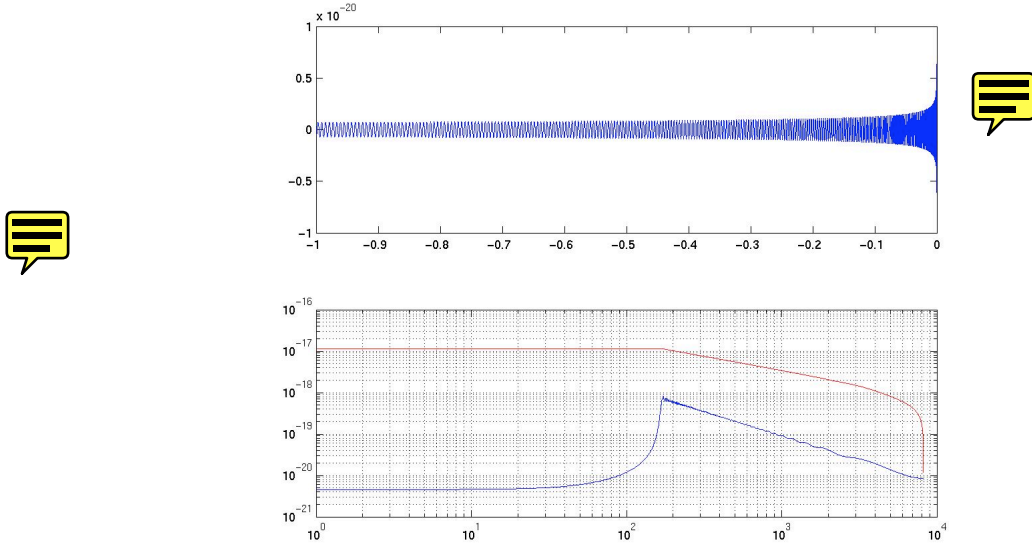


Figure 2: Chirp gravitational wave from a typical coalescence of two inspiralling compact stars: the figure on top shows the time dependency of either  $h_+$  or  $h_\times$  and the figure on the bottom shows the time dependency of the GW frequency (blue curve) and its integral (red curve). The figure is reproduced from [REF]

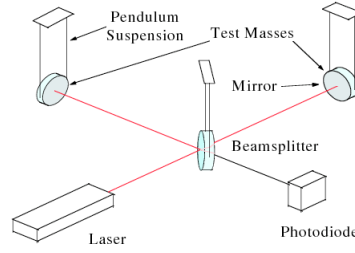


Figure 3: Schematics of a Michelson interferometer

### 3 Detectors of Gravitational Waves

There is variety in the types of gravitational waves detectors in use nowadays. The most widely used and altogether the largest type of detector uses laser light interferometry as functional principle. A simplified schematic of a Michelson laser interferometry GW detector is pictured in Figure 3.

It consists of two arms oriented at 90 degree angle with laser beams running along the length of the arms. The laser light is emitted at the centre of the L shape and split using a beam splitter, the light then travels along each of the arms, is reflected by mirrors at the end of each arm, passes back down along the arms and is recombined at the initial starting point. The principle is that as the path length for the light to travel down the arms varies, the laser light being recombined will have a variable phase difference and thus by observing the interference pattern we can measure the change in path length between the two arms.

Consider now an O-shaped string of test masses subject to the passage of a gravitational wave  $h(t) = (h_+, h_\times)$ . The effect of the + polarization is shown in Figure 4 and the effect of the  $\times$  polarization is shown in Figure 5 [REF]. The gravitational wave, when passing through the interferometer, will alter the lengths of the light arms (paths) just as the particles separation is altered in Figure 4 and Figure 5. By changing the lengths of the light paths one can get an interference pattern at the recombination point.

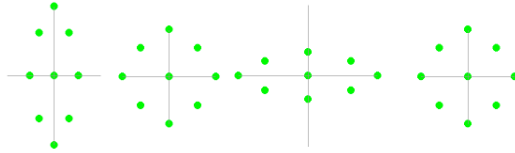


Figure 4: Effect of passage of + polarization

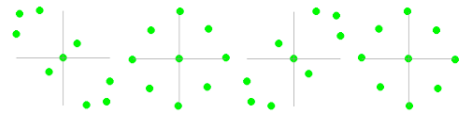


Figure 5: Effect of passage of  $\times$  polarization

**LIGO** The Laser Interferometry Gravitational Observatory (LIGO) is the largest interferometer in use as of today. LIGO operates two gravitational wave observatories in unison: the LIGO Livingston Observatory in Livingston, Louisiana and the LIGO Hanford Observatory, located near Richland, Washington. These sites are separated by 3,002 kilometers [REF]. Since gravitational waves are expected to travel at the speed of light, this distance corresponds to a difference in gravitational wave arrival times of up to ten milliseconds. Each observatory supports an L-shaped ultra-high vacuum tubes system, measuring 4 kilometers on each side. The primary interferometer at each site consists of mirrors suspended at each of the corners of the L; it is known as a special Michelson interferometer in that it recycles the power. A pre-stabilized laser emits a beam of up to 35 W that passes through a beam splitter at the vertex of the L. There, the beam splits into two paths, one for each arm of the L; each arm contains Fabry-Perot cavities that store the beams and increase the effective path length by multiple reflections.

When a gravitational wave passes through the interferometer, the space-time in the local area is altered. Depending on the source of the wave and its polarization, this results in an effective change in the length of one or both of the L cavities. This length change will bring the cavity very slightly out of resonance, and will cause the in the cavity to slightly change its phase compared to the incoming light.

After an equivalent of approximately 75 trips up and down the 4 km length to the far mirrors and reverse, the two separate beams leave the arms and recombine at the beam splitter. The beams

returning from two arms are kept out of phase so that when the arms are both in resonance (as when there is no gravitational wave passing through), their light waves subtract, and no light should arrive at the photodiode. When a gravitational wave passes through the interferometer, the distances along the arms of the interferometer are shortened and lengthened, causing the beams to become slightly less out of phase, so that some light arrives at the photodiode, indicating a signal. The  $h_{\text{rot}}/l$  is actually measured in this way, with  $\delta l/l$  the relative variation in length of the detector arms due to the passage of the gravitational wave and  $h$  the amplitude of the GW. A detector with an arm length of 4 km responds to a gravitational wave with an amplitude of  $10^{-21}$  due to an actual variation in length of about  $\delta l = 4 \times 10^{-18}$  m—this is actually the order of magnitude of the size of an atom.

In the case of a ground-based laser interferometer like LIGO, in the time-domain,  $h = h(t)$  can be written as a linear combination of its two polarizations  $h_{\times}$  and  $h_{+}$  given in equations Equation 49 and Equation 50:

$$h(t) = F_{\times} h_{\times} + F_{+} h_{+} \quad (57)$$

where  $F_{\times}$  and  $F_{+}$  are the so-called antenna factors that are functions of  $(\theta, \phi)$ , the position angles on the sky, of the binary. These two functions appear in the waveform due to purely geometrical reasons: they are introduced when rotating the reference system of the wave of the reference system of the detector. They are known for each binary system analyzed and their RMS tells us how the binary is oriented with regards to the detector. Ideally we would expect an RMS equal to 1 for a perfect overhead orientation ( $F_{+}=1$  and  $F_{\times}=0$ ). Their expressions in terms of  $\theta$  and  $\phi$  are given below:

$$F_{+}(\theta, \phi) = \frac{1}{2}(1 + \cos^2 \theta) \cos(2\phi) \quad (58)$$

$$F_{\times}(\theta, \phi) = \cos \theta \sin(2\phi) \quad (59)$$

With such small detected signals, noise plays an important role. The main sources of noise for a typical LIGO-like detector are given in [REF]:

- **Thermal noise** Thermal vibrations of the internal parts of the interferometer can mask gravitational waves. Interferometers minimise the effect of noise by measuring only at frequencies far from the resonant frequency, and making sure all materials have high quality factors, so their resonances are sharp and energy leakage to measurement frequencies is small. In terms of temperature, interferometers usually operate at room temperature.
- **Shot noise** The photons that are used to do interferometry are quantized, and so they arrive with random phases and hence make random fluctuations in the interference pattern that can look like a gravitational wave signal. The more photons one uses, the smoother will be the interference signal.
- **Ground vibration** Mechanical vibrations must be screened out. There are many different ways to do this but all of them are very sensitive to frequency, work well down to a lowest effective frequency. The most ambitious isolation system is being developed for the Virgo detector. The third generation detectors (LISA) will be space based so this problem is eliminated.

A sensitivity curve for a detector, or a noise curve, represents an  $n = n(f)$  plot where  $n$  is the detector noise and such a set of curves is pictured in Figure 6 for the LIGO observatory:

## 4 Data Analysis Procedures

### 4.1 Matched Filtering

Firstly we will (re-)introduce the Fourier transform of a function of time  $F(t)$  as denoted by  $\tilde{F}(f)$  and is given by

$$\tilde{F}(f) = \int e^{-2\pi i f t} F(t) dt. \quad (60)$$

The inverse Fourier transform will be conversely

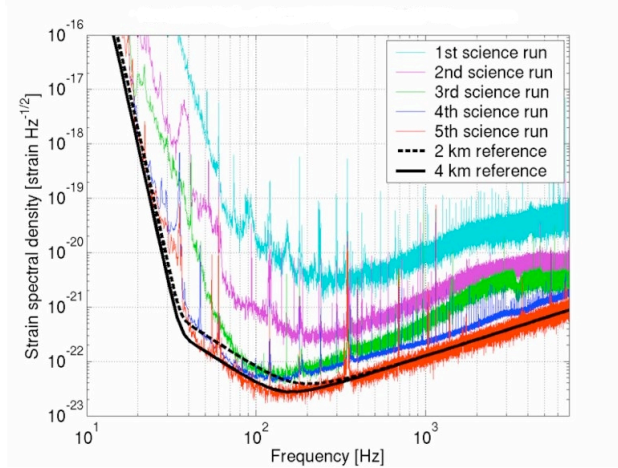


Figure 6:

$$F(t) = \int e^{2\pi i f t} \tilde{F}(f) df. \quad (61)$$

The typical gravitational wave detector output is denoted by

$$s(t) = n(t) + h(t) \quad (62)$$

where  $n(t)$  is the (real) strain-equivalent noise produced by fluctuations within the detector due to external and internal mechanical causes, and  $h(t)$  is a gravitational waveform of astrophysical origin.

The detectors noise can not be controlled or analytically generated in any way. It is purely a consequence of the internal vibrations of the detectors components (e.g. mirrors) and of the external vibrations due to environmental factors (earthquakes, passing trucks etc). There are different data channels in the detectors that monitor noise only and a lot of the spurious effects of internal and external noise are vetoed. Thus, the detector's noise  $n(t)$  can only be characterized statistically by sampling the noise data and building a noise power spectrum. For simplicity of calculations we will assume that the noise is Gaussian and stationery. This is actually close to the real case, minus the accidental peaks (glitches) that escape the veto tests. One must introduce tools for determining the expected properties of quantities measured in the presence of this noise. One can assume that  $n(t)$  is a random time-series drawn from a large ensemble of such time series, and that  $\langle n(t) \rangle$  vanishes, which implies that  $\langle \tilde{n}(f) \rangle = 0$  (white noise). This implies that the expectation value  $\langle n(t)n(t') \rangle$  depends only upon the time difference  $|t - t'| = \tau$ . It then follows that in frequency space

$$\langle \tilde{n}(f) \tilde{n}^*(f') \rangle = \frac{1}{2} S_n(f) \delta(f - f'), \quad (63)$$

where  $\delta(f)$  is the Dirac delta-function in frequency space and the real non-negative even function  $S_n(f)$  is the noise power spectral density (PSD).

The search method applied is *matched filtering*: the gravitational waveform is known apriori and expected in the detectors output, together with noise, hence, equal segments of output data and expected signal are treated as vectors and the degree of overlapping of the two vectors is given by a linear filter, or a hermitian inner product. We can consider the detector output  $s(t)$  and a signal  $h(t)$  that lasts for a duration of  $T$ . If the signal arrives at the detector at time  $t_0$ , then the detector output can be written

$$s(t) = \begin{cases} h(t - t_0) + n(t), & t_0 < t < t_0 + T \\ n(t), & \text{otherwise} \end{cases} \quad (64)$$

where  $n(t)$  is the detector noise. Introducing the filter function  $K(t)$  in the time domain, the filtered output signal  $S$  will be

$$S = \int_{-\infty}^{\infty} K(t) \langle s(t) \rangle dt = \int_{-\infty}^{\infty} K(t) h(t) dt = \int_{-\infty}^{\infty} \tilde{K}^*(f) \tilde{h}(f) df \quad (65)$$

and the noise will be

$$N^2 = \int_{-\infty}^{\infty} \int_{-\infty}^{\infty} K(t)K(t+\tau) \langle n(t)n(t+\tau) \rangle dt d\tau = \int_{-\infty}^{\infty} \frac{1}{2} S_n(f) |\tilde{K}(f)|^2 df \quad (66)$$

The signal to noise ratio is defined as  $\text{SNR}=S/N$  and the question arises which is the filter function that maximizes the SNR? By introducing a hermitian inner product between two vectors  $A$  and  $B$  as in

$$(A|B) = 4\text{Re} \int_0^{\infty} \frac{\tilde{A}^*(f)\tilde{B}(f)}{S_n(f)} df \quad (67)$$

we observe that the SNR can be written in a compact way as:

$$S/N = \frac{(s|h)}{\sqrt{(h|h)}} \quad (68)$$

and if the filter function is expressed as

$$\tilde{K}(f) = \text{const.} \frac{\tilde{h}(f)}{S_n(f)} \quad (69)$$

the SNR is maximized to

$$(S/N)_{\text{max}} = \sqrt{(h|h)} \quad (70)$$

The waveforms  $h(t)$  depend on a series of parameters:  $h = h(m_1, m_2, d, s_1, s_2, \iota, \theta, \phi, \Phi_0, t_0, f_{gw}(t))$  where  $m_{1,2}$  are the masses of the two binary components,  $d$  is the distance from the binary centre of mass,  $s_{1,2}$  are the spins of the binary components,  $\iota$  is the inclination of the binary with respect to the line of sight,  $\theta$  and  $\phi$  are the position angles on the sky (right ascension and declination),  $\Phi_0$  and  $t_0$  are the coalescence phase and time,  $f_{gw}(t)$  is the GW frequency as a function of time. Since these parameters are a continuous series, it is not possible to search at every possible parameter value for each of the binary components. However, if a signal is close enough to a template, the loss of SNR will be small. Thus, by using an appropriate set of templates, called a *template bank* in mass space, one can cover all masses in the desired mass interval with some predetermined maximum loss in SNR. The smaller the maximum loss in SNR, the larger the number of templates needed in the bank [REF]. Typically, searches will implement a template bank with a maximum SNR loss of 3 percent, which leads to template banks containing of the order of a few hundred templates (the exact number depends on the noise spectrum).

## 4.2 $\chi^2$ test

When noise is Gaussian and stationery the matched filtering technique gives the best probability to find a signal with a before-known waveform. Most of the times, though, the detector noise contains very energetic peaks (noise glitches) that affect sometimes the template bank by it rendering a high SNR to these glitches. It is necessary to have some other way of distinguishing the majority of glitches from true signals.

The method which has become standard for this is to use a *chi-squared* ( $\chi^2$ ) veto test [REF]. When a template exceeds a certain threshold SNR, it is then divided into  $p$  different frequency bands such that each band should yield  $1/p$  of the total SNR of the data if the high SNR event was a signal matching the template. The sum of the squares of the differences between the expected SNR and the actual SNR from each of the  $p$  bands, that is the  $\chi^2$  statistic, is then calculated. The advantage of using the  $\chi^2$  veto is that glitches tend to produce large  $\chi^2$  values, and are therefore distinguishable from true gravitational waves signals. Thus, only those template matches with low enough  $\chi^2$  values are considered triggers.

If the data was a matching signal in Gaussian noise, the  $\chi^2$  statistic would be  $\chi^2$  distributed with  $2p - 2$  degrees of freedom [REF]. However, it is much more likely that the template that produces the highest SNR will not be an exact match for the signal. In this case, denoting the fractional loss in SNR due to mismatch by  $\mu$ , the statistic is distributed as a non-central chi-squared, with non-centrality parameter  $\lambda \leq 2\rho^2\mu$ . This simply means that the  $\chi^2$  threshold,  $\chi^*$ , depends quadratically on the measured SNR,  $\rho$ , as well as linearly on  $\mu$ .

## 5 Short Hard Gamma Ray Burst GRB070429B analyzed by the inspiral pipeline

Gamma-ray bursts (*GRBs*) are the most luminous electromagnetic events occurring in the universe since the Big Bang. They are flashes of gamma rays emanating from seemingly random places in deep space at random times. The duration of a gamma-ray burst is typically a few seconds, but can range from a few milliseconds to several minutes, and the initial burst is usually followed by a longer-lived "afterglow" emitting at longer wavelengths (X-ray, ultraviolet, optical, infrared, and radio). Gamma-ray bursts are detected by orbiting satellites about two to three times per week. Most observed GRBs appear to be collimated emissions caused by the collapse of the core of a rapidly rotating, high-mass star into a black hole. A subclass of GRBs (the *short* bursts) appear to originate from a different process, the leading theory being the merger of neutron stars orbiting in a binary system. All observed GRBs have originated from outside our own galaxy, though a related class of phenomena, soft gamma repeater flares (SGR), are associated with galactic magnetars.

There are at least two different types of progenitors (sources) of GRBs: one responsible for the long-duration, soft-spectrum bursts and one (or possibly more) responsible for short-duration, hard-spectrum bursts. The progenitors of long GRBs are believed to be massive, low-metallicity stars exploding due to the collapse of their cores. The progenitors of short GRBs are still unknown but mergers of neutron stars is probably the most popular model as of 2007: short gamma-ray bursts appear to be an exception. Until 2007, only a handful of these events have been localized to a definite galactic host. However, those that have been localized appear to show significant differences from the long-burst population. While at least one short burst has been found in the star-forming central region of a galaxy, several others have been associated with the outer regions and even the outer halo of large elliptical galaxies in which star formation has nearly ceased. All the hosts identified so far have also been at low redshift.[11] Furthermore, despite the relatively nearby distances and detailed follow-up study for these events, no supernova has been associated with any short GRB.

### 5.1 Introducing GRB070429B

GRB070429B was a short hard  $\gamma$ -ray burst that was observed on April 29, 2007 at 03:09:04 by the Swift/UVOT satellite. Its duration was 0.500 s and its sky location was RA 328.02 and DEC -38.84. LIGO's IFO's responsible for detection were Hanford 1 (H1) and Livingston (L1). What is interesting to note is that the antenna factors  $F_{\times}$  and  $F_{+}$  for H1 and L1 are 0.99 and 0.93 respectively giving an  $F_{RMS}$  equal to 0.96 which reveals an almost overhead position with respect to H1L1 detector. Both H1 and L1 detectors were running in science mode at the time of the GRB. The astronomical and detector data summarizing the characteristics of GRB070429B is presented in Table 1.

GPS	Date	redshift	duration [s]	RA	DEC	H1	H2	L1
861851358	Apr 29 2007 03:09:04	0.904	0.43	328.02	-38.84	0.99	0.99	0.93

Table 1: Astronomical and detector data for GRB070429B

It is interesting to note that initially, in the GRB data record that LIGO is using, there was no redshift associated with this particular GRB. Nevertheless, at a closer look at the GCN circulars written on GRB070429B a possible redshift can be assigned by association with a faint object (galaxy) seen on the night of October 9, 2007, using the Keck telescope. Longslit measurements have been performed and the trace of object was found to be faint and the spectrum was mostly featureless, but a faint line signature was observed centered at 7098 Angstroms. The feature was identified as most likely being the [OII] 3727 doublet. Other line identifications ( $H - \alpha$ ,  $H - \beta$ , or [OIII]) were disfavored due to the absence of corroborating lines that would be expected over the spectral range (3500-8900 Angstroms) in those cases. Association of this feature with [OII] indicates a redshift for this object of  $z=0.904$  (luminosity distance of about 4 Gpc). Calibrating relative to R-band photometry, the estimate was a preliminary line flux corresponding to an unextincted star formation rate (cite[Kewley et al. 2002]) of  $0.7 M_{\odot}/yr$ , comparable to that observed in previous short burst hosts. The host appears to be a red galaxy [citeGCN].



## 5.2 The Data Analysis from GRB070429B

**Analysis overview and results** Analyzing data from a single GRB makes use of the same inspiral pipeline as the used during the LIGO-Virgo science runs. The major benefit of analyzing a single event well localized in time and in the sky (e.g. a single short GRB with a known trigger time and sky position) is that instead of analyzing 18 months worth of data only a short *on – source* and *off – source* times worth of data are analyzed, hence lowering the chances of missing a possible GW event and increasing the search sensitivity by having a well-defined patch in the sky to look at. The *on – source* time is centered around the trigger time of the GRB and placed at  $[-5,+1]$  with respect to the GPS trigger of the GRB, hence 6s long in duration. The off-source time is used to estimate the noise contribution in the detectors and roughly 300 segments each 6s long are analyzed. Each of these segments is called off-source trial. A number of simulated signals are injected in the off-source time-domain segments so that the response of the data in the case a signal is present can be tested. The injected signals (injections) are waveforms present in an injections template bank and the longest template is roughly 45s; as a consequence a buffer time of roughly 8 segments long (48s) is discarded on either side of the on-source time so that there is no bias inbetween a possible loud signal in the on-source and a simulation from the off-source. Additional data padding on either sides leads to a minimum analyzed time of  $\sim 2190$ s.

The detectors output, which is a time-series, will be calibrated first and then software injections will be performed in the time-domain data. The time-series data segments are then converted into frequency-series by doing Fourier transforms and then match-filtered through a bank of theoretical waveforms that replicate a real gravitational wave with frequencies within the detectors’ band. The waveforms are mathematically correct to a certain post-Newtonian approximation and they depend on the component masses of the binary system and on the other inspiral-stage parameters explained in the theory section above (inclination, polarization, etc). The match-filtering is done using a waveform template bank that is symmetric in component masses in the interval  $[1 M_{\odot}, 40 M_{\odot})$ . The number of template waveforms depends on the sensitivity of the detector and in the case of GRB070429B which was analyzed with data from H1 and L1, 6000 templates have been used for H1 and 9000 for L1. The result of match-filtering is a series of triggers with various SNRs for both H1 and L1, as seen in Figures 1 and 2. Figures 3 and 4 show the cumulative number of triggers versus SNR in H1 and L1.

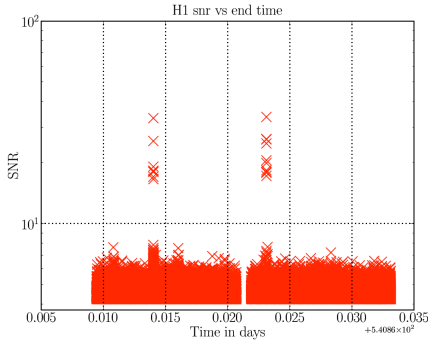


Figure 7: SNR vs. time in H1

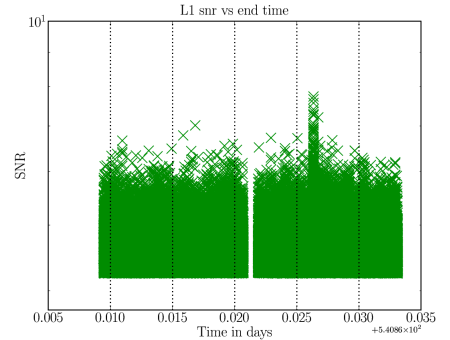


Figure 8: SNR vs. time in L1

As seen from the plots above, the data in the H1 detector has a few very loud glitches ( $SNR \geq 30$ , less than 10 glitches) whereas the data in L1 is rather smooth and lacking loud glitches. The glitches in H1 will be subsequently eliminated from the data in the next steps of the analysis. In both Figures 1 and 2 the gap inbetween the trigger clusters represents the on-source (the 6 s around the GRB trigger), which is not shown due to the possibility of finding a rather loud glitch that can be initially misinterpreted as a real GW signal.

An SNR threshold cut was applied for the triggers seen in the plots above, that is, triggers are kept only they have SNRs greater than a minimum SNR, set individually for each detector according to the available data for each GRB and that maximizes the sensitivity/computational cost ratio. The threshold SNR was set to 4.25 in the case of H1 and L1 GRB analysis. Template masses and trigger times are stored for further investigations.

Next, coincidence tests are applied on these resulting triggers. The first test uses a sliding window equal in length to the template used. The next coincidence test, called Ethinca, searches for triggers

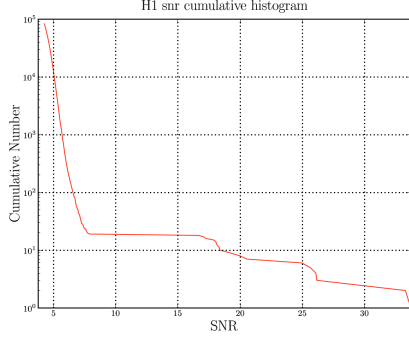


Figure 9: Cumulative number of triggers versus SNR in H1

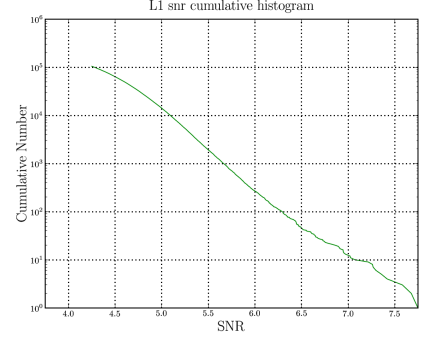


Figure 10: Cumulative number of triggers versus SNR in L1

with the same masses and trigger times that have to coincide at least in two detectors (in the case of GRB070429B it is only two detectors) and is a powerful noise exclusion tool. The Ethinca (or elliptical thinca) code is a rather new coincidence algorithm for determining if triggers from different detectors are in coincidence. It computes a three dimensional ellipse in the signal space (typically determined by the coordinates coalescence time,  $\tau_0$ , and  $\tau_3$  where  $\tau_0$  and  $\tau_3$  are two independent functions of component masses that considerably flatten the parameter metric), with a size determined by the ethinca parameter. If these ellipses overlap, then triggers are considered to be coincident. The degree of coincidence is therefore quantified by the Ethinca parameter, the smaller the Ethinca parameter is, the better a coincidence is confirmed. The threshold Ethinca parameter value above which a coincidence is no longer confirmed was set to 0.8 in the case of the GRB search. Plots of the Ethinca parameter for both H1 and L1 can be seen in Figures 5 and 6; the total number of coincident triggers is listed in the plots' legend with red dots being coincidences from injections and black crosses coincidences from sliding window triggers. The shape of the plots can be motivated by the fact that higher SNR coincident events having a lower Ethinca parameter are less likely to be found than quiet coincidences with a high Ethinca parameter.

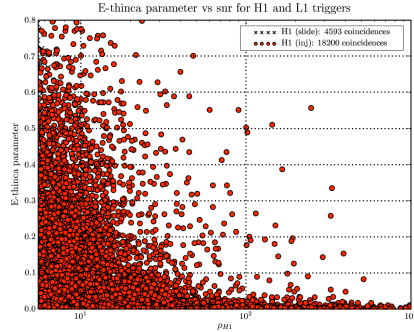


Figure 11: Ethinca parameter versus SNR in H1 detector

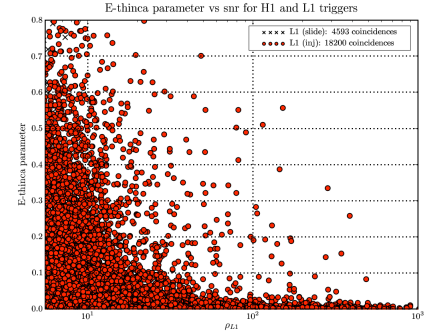


Figure 12: Ethinca parameter versus SNR in L1 detector

The triggers that survive the coincidence test are stored and component masses, coalescence phases and effective distances are computed from the templates they were matched against.

Consistency tests are then applied, such as the  $\chi^2$ , in order to differentiate between triggers consistent with a possible signal and noise triggers. The  $\chi^2$  has been qualitatively described in the Data Analysis section above. Figures 7 and 8 show the the distribution of  $\chi^2$  versus SNR ( $\rho$ ) for injections (red crosses) and for off-source triggers (blue stars). The colored continuous lines represent lines of constant effective SNR. We observe that the injections (simulated signals) follow a desired evolution in  $\chi^2 - \rho$  space maintaining a relatively low  $\chi^2$  for SNRs of up to 100, whereas the triggers jump in  $\chi^2$  values for low values of SNR.

The SNRs and  $\chi^2$  test results from each detector are combined into an effective SNR and the effective SNRs from H1 and L1 are added in quadrature to obtain a cumulative effective SNR. The effective SNR has been used as detection statistic in the S3, S4 and S5 science runs. It is a combination

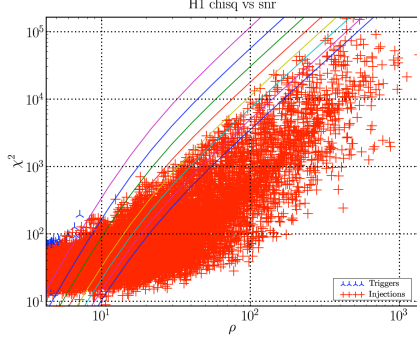


Figure 13: Chi square versus SNR for injections and triggers in H1

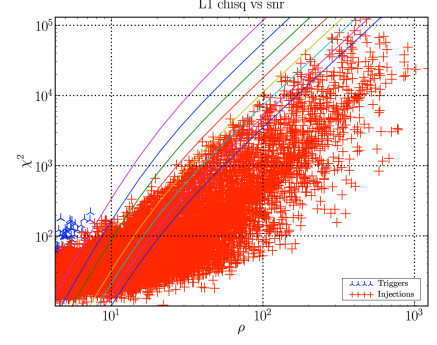


Figure 14: Chi square versus SNR for injections and triggers in L1

of the signal to noise ratio and the chi-squared value. For a signal with relatively small SNR and an average value of the chi-squared veto the value of effective snr is equal to the SNR. However, for a signal with a large chi-squared value, the effective  $\rho$  is reduced according to:

$$\rho_{eff}^2 = \frac{\rho^2}{\sqrt{(\frac{\chi^2}{2p-2})(1 + \frac{\rho^2}{250})}} \quad (71)$$

where  $p$  is the number of degrees of freedom in the  $\chi^2$  measure, here 16. The denominator 250 is chosen to best separate the background (off-source) from signal (as seen in the Chi squared plots above, the signal, represented by the red injections, separated from the blue stars, the off-source triggers).

According to their cumulative effective SNRs, the surviving triggers are gathered in a candidate list which will be partitioned in three mass bins, according to the chirp mass recovered for every candidate ( $M_c \in [0.86, 3.48)$ ,  $[3.48, 7.40)$ ,  $[7.40, 17.5)$ ). The cumulative number of candidates versus the effective SNR for the three chirp mass bins is plotted in Figures 9, 10 and 11. The subsequent candidates in their corresponding mass bins will be ranked based on a likelihood statistic and detection or upper limits are set according to this statistic.

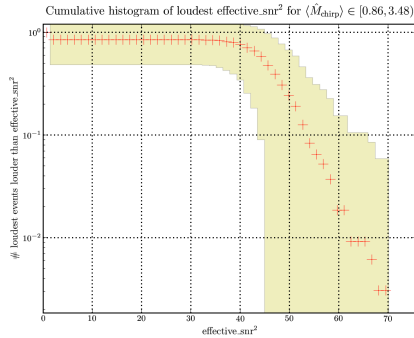


Figure 15: Cumulative no. of loudest coincident triggers in low chirp mass bin

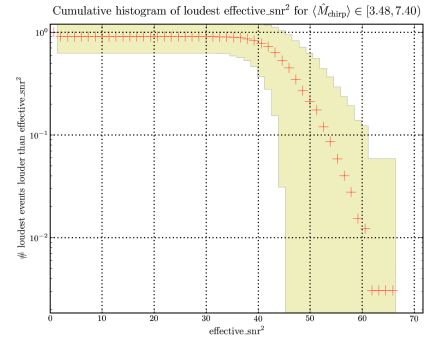


Figure 16: Cumulative no. of loudest coincident triggers in medium chirp mass bin

A very important part of the analysis and post processing of the data is injecting the simulated signals into the data, in the very initial stage of the analysis. The injections statistics folds in the final detection or non-detection statements, as seen below. Different kinds of waveforms are injected, and the majority of them are found (an injection is considered found if there is a trigger found within 100 ms of the time of the simulation; that trigger being the found injection). Reasons for not finding an injection range from the existence of a very loud detector glitch at the time of the injection, a very poor choice of parameters in the simulation (is mostly referred to high-spin simulations) and a poor recovery of the parameters (very high  $\chi^2$ ). The missed/found injections plots are shown in Figures 12 and 13. There is a cluster of loud glitches in H1 at around  $t=0.014$  s and again at around  $t=0.023$ . A glitchy peak in SNR can be seen in L1 at around  $t=0.026$  s. If we look at the found/missed

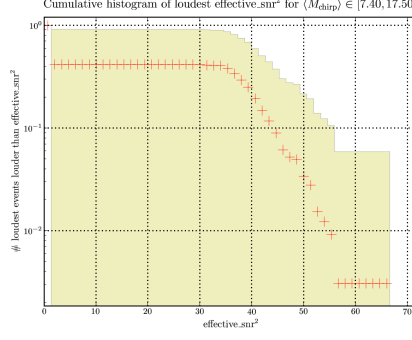


Figure 17: Cumulative no. of loudest coincident triggers in high chirp mass bin

injections plot on a time-scale we observe that in H1 there are two clusters of missed injections at exactly  $t=0.014$  s and around  $t=0.023$ . The same plot for L1 this time shows a cluster of missed injections within 5 ms of  $t=0.025$  s. Hence the conclusion is that most of the missed injections are due to glitches and spin.

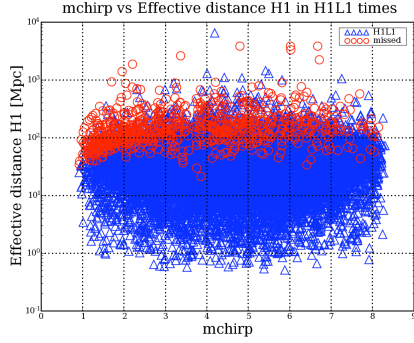


Figure 18: Found/missed injections in H1

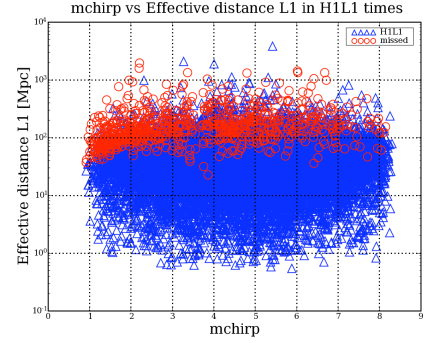


Figure 19: Found/missed injections in L1

All the analysis stages undertaken above are meant to check the data, match-filter it, model the background (the off-source, the noise), veto loud glitches and anything that is not consistent with a signal and overall making the necessary steps towards the final detection (or non-detection) stage. This stage is called opening the box and involves revealing the necessary plots that confirm or disconfirm a detection of GW. The statistic that lies behind the detection statement is a likelihood based one, described quantitatively below.

Consider the space of chirp masses divided into the three bins, as explained above. Also consider  $P(c_i(\theta_j) \in \sum_c^m | 0)$  the probability that a certain  $i$  coincident off-source event  $c_i = c_i(\theta_j)$  being a function of  $\theta_j$  parameters (combined effective SNR, masses, inclination, polarization etc) lies in the semibounded region  $\sum_c^m$  of the loudest event in each of the chirp mass bins for every of the 300 off-source trials. The region is bounded at the lower end by the loudest event (highest SNR in the chirp mass bin per trial) and at the higher end is open.  $P(c_i(\theta_j) \in \sum_c^m | 0)$  is called the false alarm probability, in other words, the probability of assigning GW signal status to a coincident event that is drawn from the set of noise triggers. This probability is a function of effective SNR and should be as low as possible in order to make a positive detection statement. The lowest value we can get in the case of the GRB search is  $1/300$  since there are 300 off-source trials.

Consider now  $P(c_i(\theta_j) \in \sum_c^m | h(\alpha_k, \beta_l))$  the efficiency of the pipeline of finding GW signals, that is, the efficiency of finding the simulations (injections) from the off-source, in other words the ratio of found over number of injected simulations. The efficiency will depend on the waveform  $h(\alpha_k, \beta_l)$  which will in turn depend on two sets of parameters -  $k$  parameters  $\alpha$  which are not to be marginalized over and hence are intrinsic to the search (luminosity distance  $D$  and companion mass  $m_{comp}$ ) and  $l$  parameters  $\beta$  that we will marginalize over with a prior distribution  $p(\beta_l)$  and hence are extrinsic to the detection statement (polarization, inclination, time of coalescence etc).

Defining now the likelihood as a function of the  $k$   $\alpha$  parameters as in the following:

$$L(\alpha_k, \rho_{eff}) = \frac{\int_l P(c_i(\theta_j) \in \sum_c^m |h(\alpha_k, \beta_l))p(\beta_l)d\beta_l}{P(c_i(\theta_j) \in \sum_c^m |0)} \quad (72)$$

Marginalization over the extrinsic parameters (also called nuisance parameters) has been done with uniform priors in the case of GRB070429B. The likelihood  $L(\alpha_k, \rho_{eff})$  is hence, after marginalizing over the nuisance parameters, a function of the only two parameters that we haven't marginalize over and effective SNR:

$$L(\alpha_k, \rho_{eff}) = L(D, m_{comp}, \rho_{eff}) \quad (73)$$

With a prior constant in volume ( $D^3 = const.$ ) we can further marginalize the likelihood and obtain a two-variable function,  $L = L(m_{comp}, \rho_{eff})$  and even more, integrate over the template companion mass space to obtain the likelihood as a function of SNR. In terms of a detection statement, one can plot a sum of  $n$  likelihoods  $\sum L_n(\rho_{eff})$  from  $n$  observed background events versus the respective SNRs and place the loudest event from the foreground (on-source) on this plot, hence comparing where it lies with respect to noise. Such a plot, part of the open box collection of plots, is shown in Figure 12 with a slightly different labelling of the axes, basically having sum of marginalized likelihoods  $\sum L_n(\rho_{eff})$  on the  $y$  axis and effective SNR on the  $x$  axis. The dotted line represents the loudest on-source event and as seen from the plot, is perfectly consistent with noise, unfortunately.

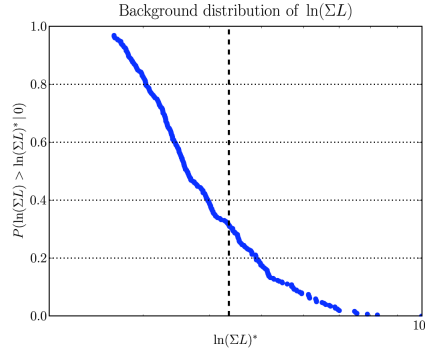


Figure 20: Background distribution in likelihood-SNR space containing the loudest foreground event

As stated above, the detection statement is based on where the observation likelihoods from the on-source lie with respect to the trigger likelihoods from the background (off-source). The open box plots of GRB070429B show this in the three chosen chirp mass bins: Figure 12 plots the false alarm rate  $P(c_i(\theta_j) \in \sum_c^m |0)$  in the  $M_{chirp} - \rho_{eff}$  space and it is visible that the lowest FAR is obtained in the high chirp mass bin, with a value of 0.117, which is by no means a satisfactory value towards a positive detection statement (since the lowest possible FAR is 1/300) and with an effective SNR of about 6.5 which corresponds to a fairly loud off-source noise trigger.

Figure 12 shows the exclusion in luminosity distance - companion mass space. The exclusion was done using an algorithm based on the Feldman-Coisins confidence belts and in the diagram the black regions are excluded 90 percent in distance, the dark grey are excluded 75 percent and the light grey are excluded 50 percent in distance.

As a conclusion to the analysis of GRB070429B, no gravitational waves have been discovered. This statement can be supported by the findings in the on-source segment: the loudest trigger with an SNR of  $\sim 6.5$  and false alarm rate of 0.117. This triggers characteristics are consistent with typical background triggers. The fact that the GRB is thought to be taken place at a luminosity distance of  $\sim 4\text{Gpc}$ , far beyond the detectors distance range, supports the non-detection statement. Placing the upper limits in distance to roughly 20 Mpc is a safe interpretation of the exclusion plots in Figure 14.

### 5.3 Future work

Data analysis from the S6/VSR2 GRBs will be performed in a semi-automated mode. I have already volunteered to be part of the GRB effort for S6/VSR2 science run and this will transcribe in a better understanding of the GRB inspiral code and continuously improving both the analysis and post=processing stages. Also, whenever the automated analysis fails, I will try and analyze the data

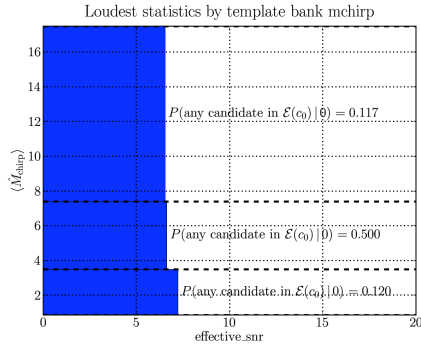


Figure 21: False alarm rate probability for the on-source segment of GRB070429B

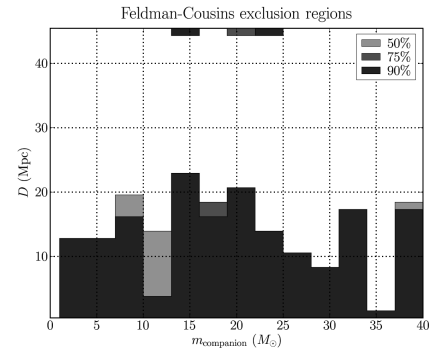


Figure 22: Exclusion in distance for GRB070429B

(as described above) manually. I have already been assigned with improving the manner in which the timeslides are performed and this will continue in the future with other pipeline improvements.

## 6 Perspectives on joint detection of GW and radio transients

### 6.1 Introduction

Coalescing binary systems of neutron stars represent one of the most promising class of sources for a future detection of GW. Apart from gravity waves, there is a whole spectrum of electromagnetic phenomena associated with such cosmic events. As in the case of short hard GRBs, supposed to originate from such mergers, gamma and optical counterparts can be easily detected. Coincident searches of GW and GRBs have already been conducted as part of S5, both by the inspiral and the burst groups, with the obvious motivation that such a search may well increase the sensitivity of the GW observations by having a defined sky location and trigger time. Another motivation for a coincident search would be that the extraction of physical parameters describing the system would be much eased.

This idea was taken further in early 2009 by establishing a new LSC group aiming at detecting coincident radio transients and GW. The newly formed Radio Analysis Group will investigate the relatively poorly observed radio universe with a series of radio telescopes in conjunction with the ongoing GW search.

In the case of binary systems of coalescing neutron stars, the available scientific literature offers a quite diverse set of theoretical models predicting a prompt radio emission either before or after the merger of the compact objects. The more numerous articles on radio signatures produced before merger in coalescing systems of two neutron stars predict observability due to the signal's extreme strength but caution must be taken due to a series of phenomena that might hinder the detection. The following chapter will summarize some of the available theoretical models and their predictions together with a brief analysis of the difficulties that might be poised against a possible radio signal detection on Earth. The models represent just a fraction of the entire literature published on this topic, and, in my opinion, are the most relevant towards the nascent effort of coincident detection of GW and radio transients.

The qualitative and quantitative analysis pertinent to these theoretical models has already been published by the respective authors and the work I have done was merely to summarize and bring the already existing papers together in one chapter of this report. The work was done in early May 2009, and a condensed version of this summary represents the theoretical backing as part of the Radio Analysis Group science case proposal. The only original work that I have done for this is in the case of relativistic magnetohydrodynamically triggered radio emissions and is included in this chapter, but not in the RAG proposal.

Apart from the discussion of theoretical radio emission models, two short subsections (one on already discovered and unidentified radio transients and the other on the follow-up analysis of such transients) will be included. The follow-up section includes a few sparse data on the LOFAR array, that will most probably furnish us with the first radio transients analyzable in conjunction with S6/VSR2 gravitational wave data.



## 6.2 Theoretical Models for radio emission before merger

**Single Pulsar Revisited** The first model described in [1] is the most basic and straightforward in terms of phenomenology. It assumes the existence of a binary system of inspiralling neutron stars with equal masses, equal radii and orbiting each other in the last phases of the inspiral in a tight circular orbit. Their spins are neglected and the existence of stellar magnetospheres is suppressed. One neutron star is a magnetar having a strong intrinsic magnetic field of the order of  $B_1 = 10^{12} - 10^{15} G$  whereas the companion has a much smaller magnetic field. The stars are modelled as perfect conducting spheres and the companion orbits in the magnetic field of the magnetar which is considered constant in the companion's reference frame. It is important to mention that the companion's orbit is well within the light cylinder of the magnetar. The magnetar's magnetic dipole  $\mu_1$  is tilted at an angle  $\alpha$  with respect to its symmetry axis. A magnetic dipole moment  $\mu_2$  is induced in the companion due to its orbiting in the magnetic field of the magnetar. The dipole  $\mu_2$  is shifted at  $R^2/a$  off the center of the companion and executes oscillations at double the orbital frequency. Poynting flux losses due to dipole oscillations carry away electromagnetic energy in the form of a coherent wave peaking its luminosity at the merger of the stars. The radiation carried away from the source has an expression given by:

$$L(t) = \frac{8\mu^2 \sin^2 \alpha \omega_{orb}^8}{3c^3 \omega_{cr}^4} \sim 5 \cdot 10^{32} \sin^2 \alpha \mu_{30}^2 t^{-3} \text{ erg s}^{-1} \quad (74)$$

where  $\omega_{cr} = \sqrt{GM/R^3}$  and  $R$  is the star's radius.

The maximum in-source luminosity is estimated in the region of  $L_{max} \sim 8 \cdot 10^{41} \sin^2 \alpha \mu_{30}^2 \text{ erg s}^{-1} \sim 8 \times 10^{41} \sin^2 \alpha \text{ erg/s}$  at frequencies in the range of kHz. The detectable flux on Earth would be around  $F_\mu \sim 5 \text{ Jy}$  for a source optimally placed at 50 Mpc.

It is important to mention that this particular model is based on a series of assumptions that may not describe correctly the real physical setting (lack of spins, lack of magnetospheres) and has only an illustrative purpose. We will further investigate more complex and closer to the real picture models. To summarize [1] predicts a coherent radio burst with a frequency of kHz, emitted shortly before merger and flux strong enough to be picked up by our radiotelescopes.

**Electron Plasma Emission** The next model described in [2] is mentioned in the LOFAR science case and cited in a series of white papers for external collaborations between gravitational waves and radio detections. It assumes the same geometrical settings as [1] only that now spins are no longer neglected - the low-field companion is a rapidly spinning recycled pulsar ( $T_2 \sim 1 - 100 \text{ ms}$ ) and the magnetar is a non-recycled slow-spinning pulsar ( $T_1 \sim 10 - 1000 \text{ s}$ ). Also, a warm magnetized low-frequency electron plasma is present inbetween the magnetar and its companion. The companion spins and rotates in the constant dipolar magnetic field of the magnetar and as a result of its rotational and orbital motion surface charges supplied from the plasma are induced on its surface. At this stage the electrodynamic system is not in an equilibrium state due to the induced charges creating strong electric fields (parallel to the magnetic field). These fields, in turn, will accelerate nearby plasma electrons in an attempt to screen the electric field and restore equilibrium. The accelerated electrons (primary beam, Lorentz factors of the order of  $\gamma \sim 10^6$ ) move along the curved magnetic lines and produce curvature radiation and a dense population of electron-positron pairs that will finally screen the companion's electric field. It is thought that 1/10 of the primary beam will be radiated within radio frequency band. The companion, now shrink-wrapped in a pair-plasma layer crosses the magnetar's magnetic field and emits Alfvén waves that may or may not escape the trap of the magnetar's magnetosphere. In the case they don't escape they will get non-linearly damped and will release all their energy in the plasma. In this case the predicted radio emission is associated with the primary beam of electrons only and it is chosen that  $\epsilon = 0.1$  of the initial beam energy is radiated in radio band at a reference frequency of 400 MHz (frequency chosen due to radio pulsar analogy). The in-source radio luminosity would be of the order of

$$L \sim 4\pi R^2 n_{GJ} \gamma_{max} m_e c^3 \sim 3.1 \times 10^{36} \text{ erg s}^{-1} \sim 3 \times 10^{35} \text{ erg s}^{-1} \quad (75)$$

where  $n_{GJ}$  is given by:

$$n_{GJ} = \frac{2\epsilon\omega B_{lc}}{e} = 3 \times 10^{18} \text{ m}^{-3} \quad (76)$$

and the flux picked up by the radiotelescopes would be

$$F_\nu \sim 2.1 \text{ mJy} \frac{\epsilon}{0.1} \left( \frac{D}{100 \text{ Mpc}} \right)^{-2} B_{15}^{2/3} a_7^{-5/2}. \quad (77)$$

and that is about 2 mJy for a source placed at 100 Mpc, having a radio energy efficiency of  $\epsilon = 0.1$ , an NS-NS separation of  $10^7$  cm and a magnetic field of  $10^{15}$  G. To bridge the first model with this more complex one, it is believed that the Poynting loss radiation is transferred to the magnetar's magnetosphere and will not escape in the surrounding ISM. Hence it is thought that the energy extraction efficiency for the primary beam (associated with the radio emission) might be significantly higher than the model's prediction.

The take-home message from this model would be that the combined effect of rotation and spin of a poorly-magnetized neutron star in the magnetic field of a magnetar (highly-magnetized neutron star) will produce strong electric fields that will in turn accelerate the charges from the stars magnetosphere to high lorentzian factors and 0.1 of the emitted radiation by these charges will be in radio frequencies. A lack of thorough understanding of the phenomenology of such a complex event as the merger of two neutron stars from the radiative point of view made the authors of this model to assign a rather loose frequency prediction - based on the fact that the phenomenon is similar to the pulsar emission mechanism, the frequency expected should lie in the 400 MHz band. The signal is expected to be emitted minutes to seconds before the merger itself.

**MHD waves induced by GW** The next model described in [3] predicts a very energetic radio transient and the emission mechanism that stands behind it is somewhat novel to the approaches discussed above. The authors postulate that a monochromatic gravitational wave when passing through a magnetized warm plasma induce magnetohydrodynamic modes. This is actually proven analytically in [4] and also described in a series of other articles ([5],[6]) and can be explained in short: the metric perturbation  $h$  induced by a GW changes the electromagnetic energy-momentum tensor and as a result a purely gravitational current density  $j$  appears in the MHD equations (see [4] for a complete derivation) which in turn produces a variation of the magnetic field that triggers MHD modes (Alfven, fast and slow magnetosonic waves, depending on the orientation of the GW wave vector with respect to the stellar magnetic field). In the scenario described in [3] the emission takes place at the light cylinder where the plasma (the extension of the magnetospheres of the two neutron stars) can no longer co-rotate with the system and hence a constant charge density can no longer be maintained (see the rotator model of single radio pulsars by Goldreich and Julian, 1968). A difference of potential is created due to a gradient in charge density and plasma electrons get accelerated to high Lorentz factors in the polar regions at the light cylinder, where the magnetic field lines are open. The electrons will move along these lines and as described in the previous model will produce a dense pair plasma that this time is unbound and will flow outwards in the form of a force-free wind with cylindrical symmetry. When the gravitational waves will pass through this pair plasma wind the force-free characteristics can no longer be maintained and MHD waves will be induced by the GW. The MHD wave will scatter on the free plasma charges and the result will be radio photons well within the detection bands of our radio telescopes. The nature of the signal predicted by [3] is an incoherent burst of radio waves around 30 MHz and with a bandwidth of 30 MHz with a duration of roughly 3 minutes for a source located at 1 Gpc. The predicted fluxes lie in the MJy region, which by may seem a little too strong, but given the very efficient damping mechanisms predicted in parallel to this model, the detected flux will most probably be much smaller. It is worth mentioning that the model discussed in [3] is a first order approximation of the relativistic MHD model derived in [4] and stands good theoretical grounds. the major difficulty in accepting such optimistic predictions lie in the very significant damping and scattering mechanisms for very bright radiation in the interstellar medium. A good description of such mechanisms is given in [7] and it is argued that heavy Raman and Compton scattering will be responsible for energy loss for bright radiative processes such as the MHD mediated one described above. A good chance to minimize the effects of scattering and absorption would be to have a well-collimated emission and this is possible in an MHD model due to efficient screening of the emission gap.

**Personal approach to MHD waves emitted due to GW-plasma interactions** A more detailed and accurate theoretical derivation of the phenomenon, available in [4] prompted me to replace the equations given in [3] and re-calculate to obtain quite spectacular results. The model is based on [3] and states that a small perturbation  $h_{ab}$  in the flat space-time metric  $\eta_{ab}$  (taken as  $(-, +, +, +)$ ), which is nothing else than the gravitational wave, has implications in generating perturbations in the



EM field. The next picture applies: two neutron stars of equal masses  $1.4M_\odot$  orbit each other with a frequency of  $\omega=1000$  rad/s in a tight inspiral orbit  $\delta t = 10^{-2}$  s before merging, still before reaching the innermost stable circular orbit (ISCO). Both stars possess strong magnetic fields and for the sake of calculations' simplicity we take the resultant field oriented along the  $x$  axis of an  $xyz$  coordinate system centered in the center of mass of the system and with  $z$  axis perpendicular to the orbital plane. The magnetic field will be  $B_0 = B_{0x} = 10^{12}$  T. This situation is more than ideal, since the orbiting stars have different orientation of their magnetic fields and the resultant field will most probably never be oriented along a preferred axis, but this way the calculations simplify in a helpful manner for a letter that is intended solely for order-of-magnitude or illustration purposes. In the most general case the orientations of the magnetic fields are important for generation of different MHD modes, in this case only one MHD mode is considered. The system will have a magnetosphere that will be consisted of electrons and ions - a warm plasma with a charge density given by the Goldreich-Julian density that according to our chosen magnetic field and orbital frequency will be given by ([2] and [3]):

$$n_{GJ} = \frac{2e\omega B_{lc}}{c} = 3 \times 10^{18} \text{m}^{-3} \quad (78)$$

where  $B_{lc}$  is the magnetic field at  $R = R_{lc} = c/\omega = 3 \times 10^5 m$ , the light cylinder radius, the boundary where the plasma is not corotating anymore, assuming a dipole-decay of the magnetic field within the light-cylinder ([2],[3],[5])

$$B(r = R_{lc}) = B_{star} \frac{R_{star}^3}{R_{lc}^3} = 4 \times 10^7 \text{T} \quad (79)$$

Temperatures in the plasma are of the order  $T = 10^6 - 10^9$  K. Also, it is worth mentioning that the charge density in the plasma might prove to be up to five orders of magnitude larger than the classical Goldreich-Julian model (according to the most recent double pulsar theories). I will take this into consideration when estimating the numerical results. The simplified geometry of the system consists of closed magnetic field lines, frozen-in the plasma, and open magnetic field lines near the poles that extend to infinity. The main radiation process will take place at the openings of the magnetic field lines. Linearized gravity and energy-momentum conservation equations, paired with Maxwell's equations written for a flat metric with a small perturbation, solved for a stationary gravitational wave  $h_{\times,+}(z, t) = h_{\times0,+0} \cos(\omega_{gw}t) \cos(k_{gw}z)$  as metric perturbation show the existence of a gravitationally-induced current density that will in turn produce a perturbation  $\delta B = \delta B(z, t)$  in the magnetic field (full analytical derivation to be found in [1]). In other words, the gravitational wave may excite Alfvén-type waves or Alfvén-type and MHD-mode (magnetoacoustic) waves in the plasma ([1],[2],[6]). For our simplified case only non-compressional shear Alfvén-waves are generated. The wave equation being a particular solution of the relativistic Maxwell equations:

$$\delta B(z, t) = \frac{B_0^3 h_{+0}}{4\pi\epsilon(1 - c_m^2)} (\cos\omega_{gw}t - \cos c_m\omega_{gw}t) \sin kz \quad (80)$$

where  $\epsilon$  is defined as the plasma total internal energy. Considering that the perturbation propagates in the plasma as an adiabatic process (there are no shocks) with index  $\Gamma$ , we have the expression for the coefficient  $c_m$  as

$$c_m^2 = \frac{\Gamma p_0 + B_0^2/4\pi}{\epsilon} = \frac{\Gamma p_0 + B_0^2/4\pi}{E_0 + B_0^2/4\pi} = \frac{v_A^2}{c^2} \quad (81)$$

where  $p_0 = k_B n_0 T_0$  is the initial plasma pressure,  $E_0 = 2\Gamma p_0/(\Gamma - 1)$  is the internal thermal energy and  $v_A$  is the Alfvén wave velocity. The above equation was written in the relativistic high-magnetic field approximation when  $v_A \gg c_{sound}$  and  $B_0^2/4\pi \gg E_0$ . It is easy to see that in this approximation the dominant mode is the Alfvén shear wave and the cosines couple to form a beats-like wave with the frequency

$$\delta\omega = \Omega = \frac{\omega_{gw} + c_m\omega_{gw}}{2} = \frac{\omega_{gw}(1 + v_A/c)}{2} = \frac{\omega_{gw}(1 + n_A)}{2} \quad (82)$$

and amplitude

$$\delta B_{max} = \frac{(\Gamma - 1)B_0^3 h_{+0}}{4\pi\Gamma k_B n_0 T_0} \sim 10^{26} - 10^{32} T \quad (83)$$

where  $k_B$  is Boltzmann's constant and  $n_0 = n_{GJ}$  is the charge density within the light cylinder. In the first order approximation ( $E_0 \ll B_0^2/4\pi$ ) we express the Alfvén velocity  $v_A$ :

$$\frac{v_A}{c} = \frac{B_0}{\sqrt{4\pi\epsilon}} = \frac{B_0}{\sqrt{4\pi(E_0 + B_0^2/4\pi)}} = 1 - \frac{4\pi\Gamma p_0}{B_0^2(\Gamma - 1)} \quad (84)$$

hence replacing above we get the frequency for the plasma waves:

$$\Omega = \frac{\omega_{gw}}{2} \frac{2B_0^2(\Gamma - 1) - 4\pi\Gamma p_0}{B_0^2(\Gamma - 1)} \quad (85)$$

We can easily see that using a rigorous derivation as in [4] we reach to the same conclusion as stated in [3] for a tenuous warm plasma in which the magnetic density of energy is much greater than the thermal energy density, in other words the Alfven wave is propagating with a slightly less speed than  $c$  and with a slightly smaller frequency than  $\omega_{gw}$ . For a simple approximation  $2B_0^2(\Gamma - 1) \gg 4\pi\Gamma p_0$  (which stands for our numerical estimates, the magnetic energy density is of the order of  $10^{14}$  whereas the pressure is of the order  $10^2 - 10^5$ ) we can easily write:

$$\Omega = \omega_{mhd} = \omega_{gw} \quad (86)$$

At the light cylinder boundary, the plasma can no longer corotate, the field lines open up and are no longer "frozen-in" the plasma and hence, charges are extracted from the initial plasma, generating strong electric fields with potential increases of the order of  $\omega_{rot}B_0 \sim 10^{15}V$  and a secondary unstable plasma composed of electrons with Lorentz factors  $\gamma \sim 10^2$  (according to [2]). As a first radiation-matter interaction, at the light cylinder, the Alfven wave will, when passing through the secondary plasma, Thomson-scatter on the free plasma electrons. This can be viewed as an inverse Compton scattering seen from a rest frame of the electrons. The primary radiation that gets scattered is a long wave radio signal that may escape the magnetosphere at this very point and be detected by ground radio telescopes but the secondary radiation resulting after scattering on the secondary plasma electrons, radio as well, will most probably be picked by telescopes such as LOFAR, strictly speaking about its frequency domain. At resonance the dispersion formula for an inverse Compton scattering reads ([2]):

$$\omega - ck\beta\cos\alpha_S = \frac{\omega_S}{2\gamma^2} \quad (87)$$

where  $\alpha_S$  is the angle between the incident radiation and the  $z$  axis of the plasma,  $\beta$  is the electron velocity,  $\omega = \omega_{mhd} = \omega_{gw}$  for a first-order of magnitude estimation and  $ck = \omega = \omega_{gw}$ . This reads that

$$\omega_S = \omega_{radio} = 2\gamma^2\omega_{gw}(1 - \beta\cos\alpha_S) \quad (88)$$

where in our simplified case when  $\alpha_S = \pi/2$  reduces to

$$\omega_{radio} = 2\gamma^2\omega_{gw} \quad (89)$$

It all boils down to the gamma factor of the scattered electrons after the interaction with the alfvenic wave. Depending on the plasma conditions the  $\gamma$  factor can be anywhere inbetween  $10^2$  and  $10^3$  and since the GW frequency is in the range of 100-1000 Hz we obtain a detectable range inbetween 1MHz and 1000 MHz, hence a radio observation of the coalescing binaries can be a fact. In terms of energetics, we can write the formula for the resulting power of an inverse Compton scatter:

$$P_{IC} \sim \frac{4}{3}\gamma^2\beta^2\sigma_T n_0 \left(\frac{dE}{dVdt}\right)_{EM}(R_{lc}) \quad (90)$$

considering that the Thomson cross-section for electrons is  $66.5 \times 10^{-30}m^2$  and

$$\left(\frac{dE}{dVdt}\right)_{EM} \sim (\delta B_{max})^2 \exp(-\mu(n_0)R_{lc}) \quad (91)$$

will give us a wave energy at the light cylinder of about  $10^{27} - 10^{31}W$  depending on the electron velocity, the absorption coefficient  $\mu$  and the final gamma factor of the radiation. Also an increase in the charge density  $n_0$  (stated in [8]) will have only an effect over the the transmission of the Alfven wave through the plasma, increasing  $\mu$ .

The problems that arise in the detectability of such a signal are related to its absorption and dispersion through the host galaxy of the binary and through the interstellar medium (ISM), as well as to spurious Compton and Raman scattering in the immediate plasma outside the light cylinder and further on, in the ISM. Strong dispersion is expected through both galactic medium and ISM. Hoping that the binary, as a very old system has drifted away from the main galactic plane, we can forget (for now) about dispersion in the galactic gas and concentrate on the propagation through the ISM. Also, the local effects immediately outside the light cylinder can be approximated to the ISM (bad one

here, needs lots more research). Dispersion through the ISM depends on the chosen density of the ISM, that is for a density of  $n_{ISM} \sim 0.1 \text{ m}^{-3}$  for a source at 100 Mpc the DM will be of  $10^7 \text{ pc, m}^{-3}$  and the delays will be of several minutes for a signal in the frequency range of 10 MHz and fractions of second for a range of 100 MHz.

### 6.3 Gamma ray burst afterglows

Inspiraling compact stellar remnants produce significant gravitational emissions, making them the favoured candidates for gravitational-wave detections. They are also likely candidates as the engine underlying short gamma-ray bursts and their associated afterglows (see also previous section). Radio afterglows likely start within tens of minutes of the initial burst, and can last for hours or days. Short hard GRBs are known for their weak afterglows, hence the impossibility of a secure confirmation of the progenitor. Results have been published on radio afterglows for SHB but the data shows only weak signals hours or days after the burst.

Several authors [?, ?, ?] have argued, in addition to afterglow from GRBs, for the prompt emission of radiation, primarily in the radio band several minutes after the observed GRB. This radio burst is predicted to have a flux on the order of mJy, which is within the sensitivity of current radio telescopes. In fact, a proposed discriminant [?] of baryon-dominated (as opposed to magnetic-field-dominated) outflows is the presence of a radio flare, stronger than the early optical afterglow, within the first half hour after the burst.

### 6.4 Unidentified radio transients

There is a series of unexplained or poorly understood radio transients, all documented in the literature. A few of them have been located near the galactic center and now bear the name Galactic Center Radio Transients or GCRT. They are relatively energetic and bursts have been detected within the 300 MHz frequency region. Amongst them, GCRT J1745-3009 is a periodic radio transient that emits  $\sim 1$  Jy pulses with a duration of about 10 minutes every 77 minutes [?]. There are a number of proposed explanations of this burst, including [?] the possibility that the bursting radio source GCRT J1745-3009 is a binary neutron star system, with at least one pulsar. Alternatively, it has been suggested that this source is a freely precessing pulsar [?] or a transient white dwarf pulsar [?].

A truly mysterious single transient was observed by Lorimer et al. [?] in 2001. At a frequency of 1.5 GHz and less than 5 ms long (believed to be intrinsically shorter, duration increases due to dispersion), this extremely bright transient was located at less than 1 Gpc distance and no host galaxy, GRB or supernova was associated with its sky location. It was detected by the Parkes telescope and based on the telescope's sky coverage the rate of such events could be as high as 200/day. This rate gives an unprecedented density of events for a joint observation effort.

So, what is the origin of radio bursts such as the Lorimer transient? Suggestions have included cusps on superconducting cosmic strings [?] and exploding primordial black holes [?], both of which would also be efficient emitters of gravitational waves. In fact, LIGO/Virgo observations could be the key to understanding the astrophysics behind such events.

### 6.5 Transients follow-up and the LOFAR telescope

Follow-up searches of radio triggers in gravitational wave data will allow us to dig deeper into the noise by focusing on short astrophysically interesting times, just as in the case of the GRB search effort, and allow us to search a small portion of the sky around the newly discovered radio transient. Therefore these searches will increase the chances of finding gravitational waves by increasing the search sensitivity in the time domain and having fixed sky locations.

An interesting aspect of follow-up of radio triggers is that for each event we will have the dispersion measure. This will provide an independent measure of the distance, and allow us to better predict when the gravitational wave should have arrived at the detectors.

The follow-up searches begin with a list of radio transients; for each one a GPS time, the duration, the energy of the burst, the dispersion measure, and sky location are recorded. For each event, one can use all available LIGO/Virgo data at the time of the event to follow up these triggers. The advantage of this method is that all the needed infrastructure (e.g. the inspiral pipeline) already exists and is being used for other triggered searches (the GRB search for instance).

There are key elements that have to be properly set before starting the search: the most important one being setting the search time window, or the on-source as explained in the GRB section above.

The setting of on-source window depends on the duration of the transient and will most properly vary from transient to transient. One has to take into consideration the fact that the intrinsic duration of the transient is much smaller than what the radio telescopes will detect, the signal being smeared in time due to dispersion. This is why the dispersion measure is very important in the search.

LOFAR (Low Frequency ARray) is a UHF antenna array currently being commissioned by a Dutch consortium lead by the Netherlands Institute for Radio Astronomy (ASTRON) and the University of Groningen. LOFAR will most probably serve as the first data source for radio transients to be followed up by the CBC group.

The instrument is currently being commissioned and first observations are slated for the end of 2009, a timescale that fortunately aligns well with S6/VSR2 science run. Briefly, the design calls for the deployment of 41 ground stations centered in the Netherlands and further stations extending throughout western Europe (for example, in Germany, France and the U.K.). Each ground station comprises an array of sensors, including between 48 and 96 each of low-band and high-band antennae having usable bandwidths of 30-80 MHz and 120-240 MHz respectively.

## 6.6 Future work

The science proposal has already been sent for review and hopefully the project will be approved. In this case, work will be done on follow-up analysis of both past and future radio transients using the inspiral pipeline. As described above, a series of prerequisites condition a smooth analysis: setting a proper on-source time, having information on the dispersion of the signal etc. When the analysis will be ready, my work will most probably consist in analyzing and interpreting results. Also, I will try to make use of the new coherent nested sampling algorithm (presented below) and follow-up on the transient triggers with it.

# 7 Nested Sampling - A New Coherent Approach

## 7.1 Introducing the Nested Sampling data analysis algorithm

Nested sampling is a Bayesian model selection analysis method and has the task to tell apart two basic models of the data  $d$ , knowing some prior information  $I$ : the noise model  $H_N$  in which data comprises of only Gaussian and stationary noise with a known PSD  $S_h(f)$  and the signal model  $H_S$  in which the data is made up of noise and a GW signal  $h = h(\theta_k)$ . Here  $\theta_k$  corresponds to the  $k = 9$  parameters that the waveform depends on: two masses, inclination, polarization, right ascension, declination, coalescing phase, time of coalescence and distance to the binary. Writing down the Bayes equation in probability functions:

$$Posterior \times const. = Likelihood \times Prior \quad (92)$$

$$P(H|d, I)P(d|I) = P(d|H, I)P(H|I) \quad (93)$$

$$P(H|d, I) = \frac{P(d|H, I)P(H|I)}{P(d|I)} \quad (94)$$

and inserting the two data model cases, we read:

$$\frac{P(H_S|d, I)}{P(H_N|d, I)} = \frac{P(d|H_S, I)P(H_S|I)}{P(d|H_N, I)P(H_N|I)} = \frac{P(H_S|I)}{P(H_N|I)} \times B_{SN} \quad (95)$$

This explained - the product of the prior odds ratio  $P(H_S|I)/P(H_N|I)$  and the Bayes factor  $B_{SN} = \frac{P(d|H_S, I)}{P(d|H_N, I)}$  is the ratio of the marginalized likelihoods of each hypothesis. The product of the prior odds ratio  $P(H_S|I)/P(H_N|I)$  represents how much confidence we start off with that a certain event is a GW signal and can be henceforth interpreted as a False Alarm Rate (FAR). For a detection to be validated or not this FAR needs to have an upper bound, beyond which detection can no longer be claimed. I will refrain from discussing this due to lack of knowledge (as of yet).

The nested sampling code, as written and developed by John Veitch from Birmingham University and described in [REF], will hopefully be used in the LSC as a fully-coherent Bayesian pipeline with the same tasks as the inspiral or burst pipelines. The code developed by John may be used to either reveal a detection or to set upper limits in the case of a non-detection. Also, it is a powerful parameter

estimation toolbox and can be used on its own or in conjunction with the inspiral pipeline for a better confidence in parameter evaluation. I have not yet the expertise to either comment on or describe the code itself but I will try to briefly summarize the main approach to the nested sampling data analysis routine and the preliminary results obtained after running the code on actual GW data from my previously analyzed GRB070429B.

The data to be analyzed is copied onto the desired machine(s) to be used with aid of the familiar *LSCDATAFIND* function of LAL. The nested sampling code itself resides in the LALapps and can be used without a special installation. The call for the code is *LALAPPS\_INSPNEST*. The only requirement is a clean installation of LAL/LALapps.

The noise PSD of the data is chosen by computing the mean power spectral density  $S_h$  using 2048 s of data from the H1 interferometer with a sampling frequency of 1024 Hz. This power spectral density is then used to generate random complex data points  $n(f_i) = n_i$ , each of which had variance  $\sigma_i^2 = (1/2)TS_h(f_i)$ , where  $T$  is the length of the segment of observation.

In the  $H_N$  model data will be only noise  $d_i = n_i$  and in the  $H_S$  model data will be noise and GW signal  $d_i = h(\theta_k)_i + n_i$ . For a Gaussian draw of the data, the Bayes factor  $B_{SN}$  will have the expression:

$$B_{SN} = \frac{\Pi[2\pi Re\sigma_i Im\sigma_i]^{-1} \exp(-\frac{|d|^2}{2\sigma_i^2})}{\int p(\theta_k|H_S, I) \Pi[2\pi Re\sigma_i Im\sigma_i]^{-1} \exp(-\frac{|d-h(\theta_k)|^2}{2\sigma_i^2}) d\theta_k} \quad (96)$$

where  $p(\theta_k|H_S, I)$  is the prior probability distribution function of the parameter space  $\theta_k$ .

Integration over the parameter space proves out to be very computationally costly due to the wide range of parameter values involved and here is where the nested sampling algorithm comes in handy to reduce the computational strength needed. This allows the calculation of the integral in reduced time by means of a probabilistic approach, whereby the prior distribution on the parameter space is stochastically sampled within a region bounded by constant likelihood. The likelihood bound is iteratively increased as the integration progresses until eventually the entire posterior distribution is covered. A good theoretical introduction to this technique can be found in [Skilling].

## 7.2 *LALAPPS\_INSPNEST* on data from GRB070429B - preliminaries

The main quantitative output of the code is the Bayes factor ( $\log_{10} B_{SN}$ ). Chirp mass, distance to the source, sky position and a series of other statistical parameters are also retrieved from the analysis. The magnitude of  $\log_{10} B_{SN}$  may tell us to a certain degree of trust if we have a detection or not. There is no proper certitude or incertitude with respect to this but a large enough  $B_{SN}$ , typical for a loud injection for instance, can suffice for a positive detection statement. Converseley, a small  $B_{SN}$ , typical for detector noise triggers, can deny a detection claim.

My main task as of yet, concerning the use of the nested sampling code, is to calibrate it, hence to map the main output of the code (the Bayes factor) and check the recovered parameters (chirp mass, distance and sky location) against the inspiral pipeline dominant statistic (effective SNR) and recovered parameters. By doing this, coincident IFO triggers, single IFO glitches, loud and quiet injections and even a full 6-s on-source of my GRB have been run and the results are compared to the ones gathered when the GRB was analyzed by the inspiral pipeline (please see previous sections). The ultimate calibration result would be an ROC plot of Bayes factor-effective SNR. This would show the

**Loud Coincident Triggers** The first set of *lalapps.inspnest* runs have been done on a set of off-source coincident triggers (in H1 and L1) with cumulative effective SNRs of 6-7 (corresponding to the loudest off-source coincident triggers). The triggers have been obtained running the command:

```
lwtprint < file_second_thinca > -t snrl_inspirall -c snr,end.time,end.time_ns,event_id,ifo > times.txt
```

Where *< file\_second\_thinca >* is the second thinca file containing the coincident triggers from the two IFOs.

The first observation I can make is that the  $\log_{10} B_{SN}$  factor is consistent in relative magnitude with the loudness of the triggers measured in effective SNR and it doesn't show steep changes. Also

Event No.	SNR H1	SNR L1	eff SNR	ChiSq H1	ChiSq L1	$\log_{10} B_{SN}$
1	4.604	4.648	6.75	31.834	19.378	1.3414
2	5.030	5.211	7.40	34.963	18.953	1.8627
3	5.155	4.336	6.89	30.616	19.564	5.4001
4	5.055	4.408	7.16	28.148	16.032	2.5248

Table 2: SNR and Bayes factor for four loud coincident off-source triggers

Run No	IFO	SNR	GPS	IFO data	GPS nested	log Bayes Factor
1	H1	33.291	861850727.478	H1L1	861850727.481	190.1569
	H1	33.291	861850727.478	H1	861850727.480	239.3139
	L1	n/a	861850727.478	L1	861850727.527	0.4288
2	H1	33.803	861851513.685	H1L1	861851513.678	244.3449
	H1	33.803	861851513.685	H1	861851513.678	271.3055
	L1	n/a	861851513.685	L1	861851513.693	-0.8759

Table 3: Results from running *lalapps\_inspnest* on two H1 loud glitches

the recovered distances place the events far away, further than the detectors detection range, implying that we are dealing with noise. The results are shown in Table 2.

**Single IFO Glitches** The next step undertaken was to test the code on very loud single IFO glitches. The loudness of single glitches can tell us a lot about the search method sensitivity. Glitches with effective SNR greater than 30 were found only in the H1 detector using the

*lwtcut H1\_INSPIRAL\_FIRST\_CAT1 -t snr > 30 -o h1.cut*

*lwtprint h1.cut -t snr,end\_time,end\_time\_ns,event\_id,ifo*

set of command lines, run on the *CAT\_1* first inspiral file available from GRB070429B.

Unfortunately the nested sampling analysis found the H1 glitches (listed below) and assigned very high Bayes factors to them even though data was analyzed from L1 as well where there was no loud event in coincidence with H1. With a more careful approach, data was analyzed again at the very same time of the glitch, but separately in H1 and L1 and we can clearly see that there was nothing found in L1 and the event in H1 looks even louder this time. As a conclusion, the search performed well in finding the glitch itself but is unbalanced in that it assigns high confidence levels to single IFO glitches. A cut test is obviously necessary in this case. Work is undergoing on this matter from Johns side and the first idea of a test cut would be to actually test the coherence of the trigger, knowing that glitches are not coherent signals. The results from running the nested sampling code on the two H1 glitches are presented in Table 3.

**Loud Injection** A loud injection was tested next, with *lalapps\_inspinj* the builder for the injection. Since a comparison to the inspiral pipeline is needed as a final result of the calibration process for the nested sampling algorithm, an existing loud and found injection from GRB070429B *injections32* (trial 1905) was chosen and because the nested sampling code works best with GeneratePPN waveforms, the spin injection 1905 was remodelled as a GenPPN waveform. The injected parameters are kept the same and only the waveform is changed. The results obtained from running the nested code are present in Table 4 with a comparison with the inspiral pipeline recovered parameters in Table 5.

GPS time (GC)	Log Bayes factor	Distance (Mpc)	Chirp mass
861851338.025	382.3053	13.6314	4.5808

Table 4: Results from running *lalapps\_inspnest* on *injections32\_Trial1905* loud injection

Injected parameters	Nested recovered	<i>sngl_inspiral</i> H1	<i>sngl_inspiral</i> L1
$M_c=4.31557417$	$M_c=4.58076998513$	$M_c=4.622$	$M_c=4.574$
$M_1=1.04274201$	$M_1=1.197 - 1.200$	$M_1=1.285$	$M_1=1.253$
$M_2=36.8460503$	$M_2=34.80 - 34.85$	$M_2=32.131$	$M_2=32.482$
$d=9.24997616$ Mpc	$d=13.6314519597$ Mpc	eff $d=24.262$ Mpc	eff $d=25.189$ Mpc
	log Bayes=382.3	$SNR=23.989$	$SNR=22.527$
		chisq=246.939	chisq=184.058

Table 5: Comparison between injected, nested sampling and inspiral (for H1 and L1) pipeline recovered parameters

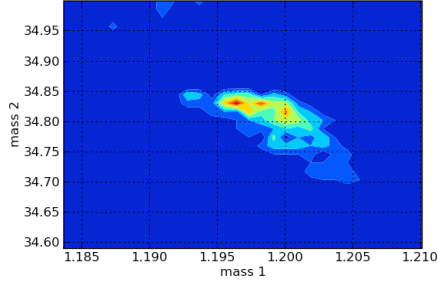


Figure 23: Parameter estimation for the recovered component masses  $m_1$  and  $m_2$  from the loud injection 1905

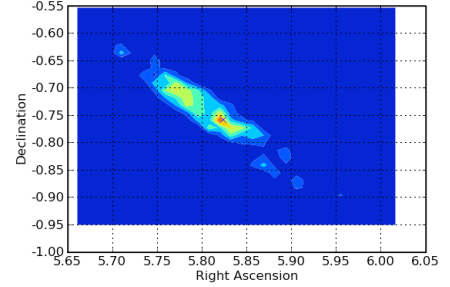


Figure 24: Parameter estimation for Right Ascension and declination from the loud injection 1905

As seen from Figures 14 and 15 there are a series of improvements to the code that will be undertaken in the future: first a color scale for the probability in both  $m_1m_2$  and  $RAdec$  plots will be introduced so that the reader gets a better feeling of the results confidence; second sky localization in the simulation run can now be specified with  $-GRB$  mode and  $-RA - dec$  flags so that the code will look for a signal in a rather narrow sky window, not as in Figure 15 where the window is very large. As seen both in the tables above and in Figures 14 and 15 the injection is found with a rather large Bayes factor and the parameter recovery looks to be more exact in the case of nested sampling analysis.

**Quiet Injection** The milestone for the Bayesian nested sampling code is the capability of finding and assigning signal status to a quiet simulation, that has an SNR comparable to the SNRs of loud-est background triggers. After injecting several waveforms with different parameters, all having a recovered effective SNR of around 6-7, corresponding to background coincidences, the retrieved Bayes factors obtained vary in the region of Bayes factors from loud off-source events. This is, of course, unsatisfactory, hence a better investigation and/or a change in the code is necessary. It is obvious that by increasing the number of live points that the search is using, the sensitivity is increased, altogether with an increase in noise contribution. This, corroborated with running in  $-GRB$  mode that limits the search on a narrow patch of sky around the specified GRB location may improve the capacity of finding such quiet signals.

I have tested the code on a quiet injection in  $-GRB$  mode with an increase in the number of sampling points from 500 (the standard number used for the tests above) to 2000 and again, in the post-processing stage the number of live points was varied from 500 to 10000 in steps of multiplicity 2. For every increment of the number of sampling points there is an increment of the Bayes factor and a decrease in the precision with which the injected parameters are recovered. This is explained by the fact that the more data points are taken the more noise is analyzed as well. The table and plots below summarize the test results: Table 6 contains the injected parameters, Table 7 contains the recovered Bayes factors, chirp masses and inclinations and Figures 19 to 24 contain the  $m_1 - m_2$  and  $RA - dec$  parameters for different numbers of live points in the post-processing mode.

The overall results obtained from analyzing this particular quiet injection are not satisfactory: the nested sampling code failed to find it as a potential GW signal, even though the recovered parameters fairly correspond to the ones injected. There is an obvious undersampling of the low mass end and John Veitch is aware of this and currently working on a solution. As a next test, the initial mass limits

SNR	Waveform	Distance (Mpc)	$M_1$	$M_2$	$M_c$	RA	dec	$\iota$	Pol
7.05	GenPPN2PN	19.75	1.43	2.52	1.64	5.71	-0.68	1.60	0.95

Table 6: Injected parameters for a quiet injection

$N$ live	$\log B_{SN}$	$M_c$	$D$ (Mpc)	$\iota$
500	-12.94	2.63	74.04	1.57
1000	-6.13	2.61	75.85	1.57
5000	7.21	3.32	84.15	1.62

Table 7: Recovered  $\log B_{SN}$ ,  $M_c$ , distance  $D$  and inclinations  $\iota$  for  $N = 500$ ,  $N = 1000$  and  $N = 5000$  live points

on which the code works will be decreased, hence narrowing the mass search window and hopefully decreasing the low mass undersampling.

### 7.3 Future work

Future work from my side will comprise of thoroughly understanding the C code in which the nested sampling algorithm is written in, continuing the calibration tests for another quiet injection narrowing the masses search intervals this time and work on overall minimizing the computational costs of the algorithm. One idea raised by Dr. Stephen Fairhurst to decrease the analysis times would be to use the code as a follow-up in both GRB and radio transients searches and Taylor expand the prior distribution assuming that the inclination of the binary is a small angle. This would significantly simplify the integral in denominator in equation (39) and will hopefully make the analysis shorter.



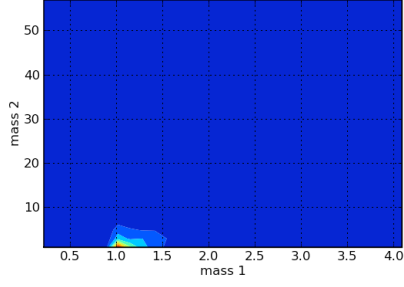


Figure 25: Parameter estimation for the recovered component masses  $m_1$  and  $m_2$  for  $N = 500$  live points

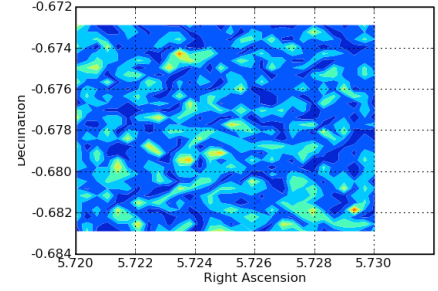


Figure 26: Parameter estimation for Right Ascension and declination for  $N = 500$  live points

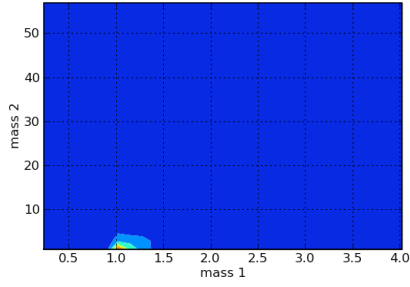


Figure 27: Parameter estimation for the recovered component masses  $m_1$  and  $m_2$  for  $N = 1000$  live points

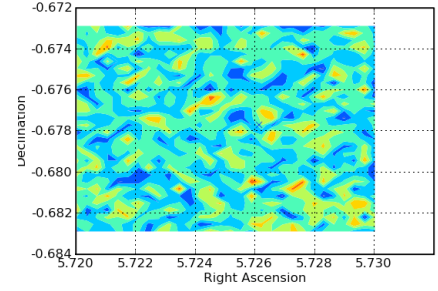


Figure 28: Parameter estimation for Right Ascension and declination for  $N = 1000$  live points

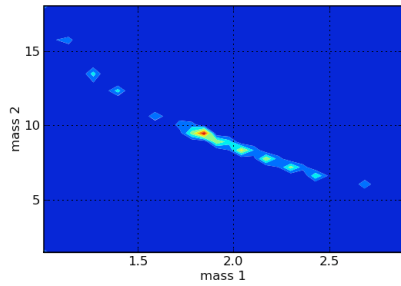


Figure 29: Parameter estimation for the recovered component masses  $m_1$  and  $m_2$  for  $N = 5000$  live points

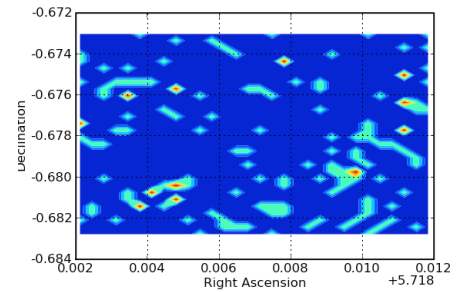


Figure 30: Parameter estimation for Right Ascension and declination for  $N = 5000$  live points